Exploring the physics of a high-performance H-mode scenario with small ELMs at low collisionality in JET-ILW

E. de la Luna[1], J. Garcia[2], M. Sertoli[3†], P. Lomas[3], S. Mazzi[2], Ž. Štancar[3], M. Dunne[4], N. Aiba[5], S. Silburn[3], M. Faitsch[4], G. Szepesi[3], F. Auriemma[6], I. Balboa[3], L. Frassinetti[7], L. Garzotti[3], S. Menmuir[3], D. Refy[8], F. Rimini[3], E. R. Solano[1], C. Sozzi[9], M. Vecsei[8] and JET contributors*

[1]Laboratorio Nacional de Fusión, CIEMAT, Madrid, 28040 Spain
[2]CEA, IRFM, F-13108 Saint Paul-lez-Durance, France
[3]UKAEA, Culham Science Centre, Abingdon, OX14 3DB, UK[†]
[4]Max-Planck-Institute for Plasma Physics, D-85748 Garching, Germany
[5]National Institute for Quantum and Radiological Science and Technology, Naka, Ibaraki 311-0193, Japan
[6]Consorzio RFX-CNR, ENEA, INFN, Universitá di Padova, Padova, Italy
[7]Division of Fusion Plasma Physics, KTH Royal Institute of Technology, Stockholm, Sweden
[8]Centre for Energy Research, Budapest, 112, Hungary
[9]Instituto per la Scienza e Tecnologia dei Plasmi-Consiglio Nazionale delle Ricerche, Milano, Italia
*See author list of "Overview of JET results for optimising ITER operation" by J. Mailloux et al., Nuclear Fusion 62 (2022) 042026
[†] Current address: Tokamak Energy Ltd., Abingdon, United Kingdom

E-mail: elena.delaluna@ciemat.es

Abstract. A new H-mode regime at low density and low edge safety factor (q_{95}=3.2, with I_p=3 MA) that combines high energy confinement, stationary conditions for density and radiation and small Edge Localized Modes (ELMs) have been found in JET with the ITER-like wall (with Be in the wall and W in the divertor). Such a regime is achieved by operating with no gas dosing, leading to a decrease in the edge density and a substantial increase in rotation and ion temperature in both the pedestal and the core region. Transport modelling shows a reduction of the turbulence across the plasma cross-section, starting from the pedestal region, and outward impurity convection, consistent with the improved energy confinement and the lack of W accumulation observed in those conditions. In addition, large type I ELMs, typically found in gas-fuelled plasmas, are replaced by smaller and more frequent ELMs, whose appearance is correlated with a substantial reduction of the pedestal density and its gradient. Pedestals in this operating regime are stable to peeling–ballooning modes, consistent with the lack of large ELMs. This is in contrast to results in unfuelled JET-C plasmas that typically operated at higher pedestal densities and developed low frequency, large type I ELMs, thus pointing to the low density as one of the critical parameters for accessing the small ELMs in JET. This small ELMs regime exhibits the same low pedestal collisionality ($\nu^*_{e,ped} \sim 0.1$) expected in ITER and operates at low q_{95}, thus making it different from other small ELMs regimes that are typically obtained at higher q_{95} and higher pedestal collisionality. These features make this newly developed H-mode regime in JET-ILW a valuable tool for exploring the underlying transport, the different mechanisms of turbulence stabilization,

as well as the physics associated with the appearance of small ELMs in high-temperature plasmas at ITER relevant pedestal collisionality.

1. Introduction

Large Edge Localized Modes (ELMs), so-called type I ELMs, typically found in high-performance H-mode plasmas, have been identified as a critical challenge to address in high fusion power operation in ITER. Type I ELMs are macroscopic magnetohydrodynamic (MHD) instabilities, which periodically relax the steep pressure gradient developed in the narrow transport barrier formed at the plasma edge of the H-mode plasmas, known as pedestal, leading to the expulsion of particles and heat outside of the plasma confined region. By flushing out main ions and impurities from the edge region, ELMs provide a mechanism to maintain the density and plasma radiation in stationary conditions in H-mode plasmas. However, the transient heat fluxes associated with large type I ELMs can rapidly erode plasma facing material surfaces, which is unacceptable in a fusion power reactor. Predictions for the Q=10 baseline scenario in ITER show that if ELMs are left unmitigated, they may severely damage the plasma facing components[1]. This has motivated the exploration of H-mode regimes that combine good energy confinement with benign heat loads to the plasma-facing components. Possible candidates are naturally ELM-free regimes that have been investigated in different devices, such as the QH-mode and the I-mode (see [2] for a recent review) and ELM suppression using externally applied resonant magnetic perturbations (RMP)[3, 4, 5, 6]. Another alternative proposed is the use of plasma scenarios with natural small ELMs such as grassy ELMs, achieved in JT-60U [7], JET with the C-wall (JET-C) [8], EAST[9] and in DIII-D[10], or the *quasi-continuous exhaust* (QCE) regime developed in ASDEX-Upgrade(AUG)[11]. However, such regimes have been obtained in narrow operational windows that do not match all the ITER relevant parameters[2]. For example, grassy ELMs are typically obtained in a small region of the parameter space at high poloidal beta ($\beta_{pol} \geq 1.1$), which is defined as the ratio of kinetic pressure to poloidal magnetic pressure, typically associated with high edge safety factor ($q_{95} > 4$). As usual, q_{95} is the safety factor at the 95% magnetic flux surface. In general, grassy ELMs are achieved at medium to high pedestal collisionality ($\nu^*_{e,ped}$ =0.5-1.5), except in JT-60U[12] and more recently in DIII-D[10], where compatibility with low collisionality operation ($\nu^*_{e,ped}$ <0.2) has been reported. The use of strong gas injection and closeness to a double-null configuration appears to be required for access to the QCE regime and, since this is a regime characterized by high pedestal density, is also limited to operation at high pedestal collisionality above the ITER target.

In addition to the need to mitigate or eliminate the large type I ELMs, an effective impurity control capable of maintaining the high Z impurity concentration as low as possible in the core region (in the range of 10^{-5}) is another essential requirement for achieving ITER goals. Operational experience in metal wall devices, as is the case for AUG[13] or JET with the ITER-like wall (JET-ILW)[14], has shown that stationary H-mode operation typically requires the use of gas puffing to ensure sufficiently high ELM frequency to efficiently flush out impurities from the pedestal region. This prevents the accumulation of impurities in the core (tungsten(W) in the case of JET or AUG), reducing the risk of plasma disruptions. The use of additional gas dosing has proven successful in controlling the W influxes through the pedestal into the core plasma but also leads to reduced pedestal temperature and, consequently, lower plasma confinement.

Since the H-mode pedestal provides the boundary condition for the core plasma performance, exploring H-mode regimes using low gas injection levels while at the same time maintaining good enough energy confinement in stationary conditions was one of the main research lines in the 2019 experimental campaigns at JET, in preparation for the deuterium and tritium campaign performed in 2021 (DTE2). This effort led to the development of a high-performance baseline scenario at low triangularity, low q_{95} (q_{95}=3.2, with $\beta_{pol} < 1$) and a mixed ELM regime, dominated by the presence of small ELMs, which is achieved by optimizing the gas injection into the plasma, replacing part of the gas dosing with pellets [15, 16]. This enabled access to higher pedestal top temperatures and thus lower pedestal collisionalities ($\nu^*_{e,ped}$ ~0.37)[17] than those obtained in standard gas fuelled baseline discharges. It is important to emphasize that, in those conditions, the confinement enhancement factor relative to the IPB98(y,2) scaling law [18] reached values of $H_{98} \sim 1$, with β_N=1.8 [17], thus simultaneously matching the edge safety factor and the confinement targets of the ITER baseline scenario, which is the reference scenario for Q=10 operation.

Moreover, the good confinement properties and the substantial reduction in ELM size were achieved in stationary conditions for density and radiation, with no core W accumulation. This small ELMs regime is sometimes referred to in the literature as the *Baseline Small ELMs* (BSE) regime[17] to highlight operation at high plasma current (3-3.5 MA), $\beta_{pol} < 1$ and low q_{95}, which distinguish it from other small ELMs regimes, such as the grassy ELMs or the QCE regime, that typically operate at higher q_{95}.

The work presented in this paper extends the existing work on the baseline scenario in JET by exploring the physics of small ELMs in plasmas with more ITER relevant, lower pedestal collisionality. Our analysis focuses on a high-performance H-mode regime developed during the 2019 campaign in JET obtained using no external gas puffing, which exhibits high pedestal top temperature and low pedestal collisionality combined with small ELMs, good density control and no W accumulation. At the lowest density achieved, the pedestal top collisionality reached values of $\nu^*_{e,ped}$ ∼0.1, which is amongst the lowest pedestal collisionality ever achieved in JET-ILW and is very similar to the range expected in ITER. It is important to highlight that this is the first time this scenario has been tested in JET with the ITER-like wall since low gas operation in metal-wall devices is quite challenging due to the associated risk of developing high-Z impurity accumulation in the core region. In fact, the unfuelled baseline scenario was initially designed to promote core impurity accumulation in view of investigating W control mechanisms for disruption avoidance. But contrary to our initial expectations, this newly found H-mode regime demonstrated the ability to maintain constant plasma density and radiated power levels while at the same time exhibiting smaller ELMs than those obtained in a conventional ELMy H-mode at higher gas dosing. In this paper, we report on initial results from such an operating regime in JET-ILW that will be referred to as the 'no-gas' BSE regime, since it is an extreme case in the generic family of the BSE operating regime, *i.e.* H-mode plasmas in the baseline scenario (q_{95} ∼3, $\beta_{pol} < 1$, β_N=1.8 and $H_{98} = 1$) with small ELMs. As such, it is a noteworthy member since it enables access to the low pedestal collisionality anticipated in ITER. The main motivation of the present work is to profit from the unique characteristics of this regime and investigate the pedestal physics, the onset conditions for small ELMs and transport properties in high-temperature plasmas at low pedestal collisionality, plasma conditions which are not easily achieved in metal wall devices.

The remainder of this paper is structured as follows: an overview of the experimental conditions and plasma performance characteristics of the 'no-gas' BSE scenario is given in section 2, focusing on key aspects that differentiate this regime from the conventional type I ELMy H mode. The role of the edge plasma density and collisionality in the access to the small ELMs is examined in section 3. The reduction in ELM size is accompanied by a reduction in the transient divertor heat loads, which is documented in section 4. Small ELMs have been observed in unfuelled H-mode plasma in JET with the ILW but not with the C-wall. The impact of the wall materials in the access to small ELMs in JET is discussed in section 5. The pedestal structure and stability of the small ELMs regime are presented in section 6. In section 7, the plasma impurity composition and impurity transport are discussed, while the turbulent transport modelling results are summarized in section 8. The discussion of the results and plans for future work are presented in section 9.

2. Characteristics of the 'no-gas' baseline H-mode scenario with small ELMs

2.1. Description of the experiment

All discharges described here were run using the same plasma shape, current (I_p = 3 MA), and toroidal field (B_T=2.8 T), with q_{95} ∼3.2. The experiments were performed in a low triangularity (δ_{av}=0.2), lower-single null X-point plasma shape, with B_T in the '*favourable*' direction for access to H-mode, *i.e.* with the ion $B \times \nabla B$ drift direction towards the main X-point. A divertor geometry with both strike points located in the divertor corners, adjacent to the pumping duct entrance, was chosen as it provides optimal pumping conditions and facilitates density control. The plasmas were predominantly heated by neutral beam injection (NBI) with a small fraction of the total heating power (3-4 MW) provided by centrally deposited ion cyclotron resonant heating (ICRH), applied in the fundamental hydrogen minority heating scheme.

The main characteristics of the unfuelled BSE regime explored in JET are illustrated in figure 1. Here, time traces of selected engineering and physics parameters for two of the best examples of this new operational regime (#94900 and #94442) are compared to those of a conventional ELMy H-mode discharge (#94777) that uses higher gas dosing levels ($\Gamma_D = 2 \times 10^{22}$ s^{-1}) during the main heating phase. The discharges #94900 and #94777 were obtained using similar heating power, comprising 21-22 MW of NBI and up to 4 MW of ICRH, while #94442 was obtained at slightly reduced heating power (P_{NBI}=17.5 MW, P_{ICRH}=3 MW). The figure includes the total input power (P_{IN}) and radiated power excluding the radiation from the divertor region (P^{bulk}_{RAD}) in panel (a), and the line averaged electron

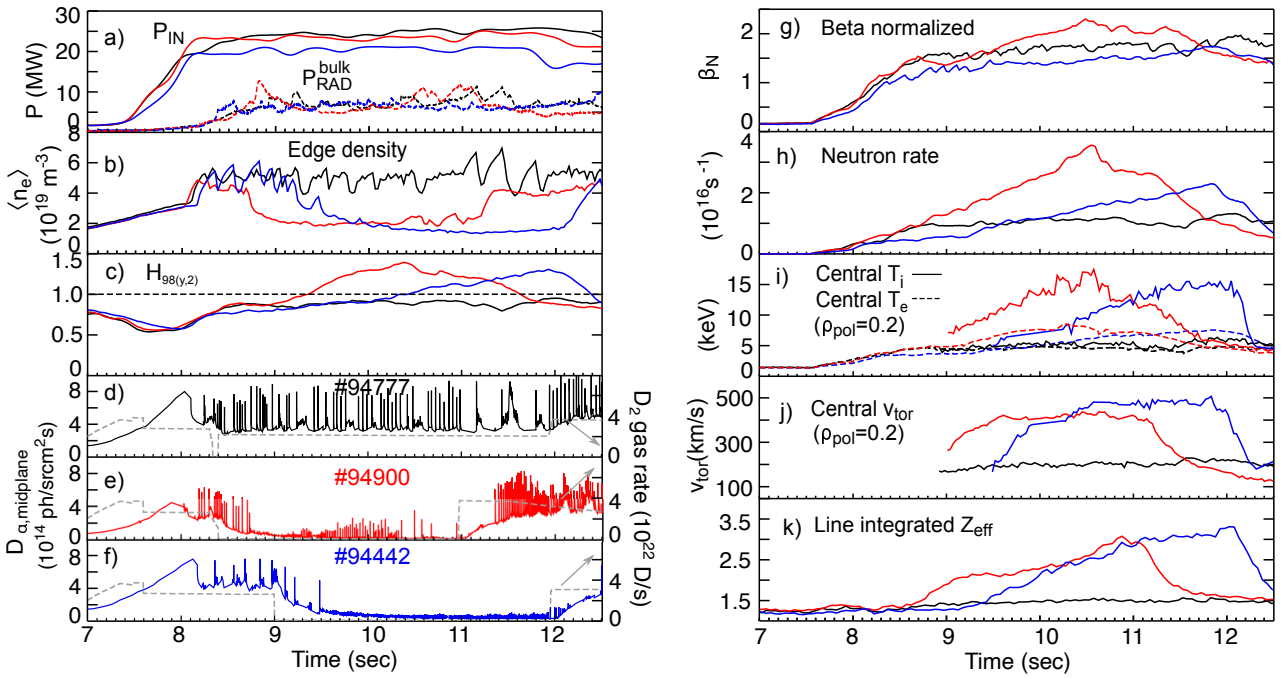

Figure 1. Comparison of a 'no-gas' BSE discharge (#94900) with a conventional ELMy H-mode references (#94777) with the same engineering parameters (I_p=3 MA, q_{95}=3.2, low δ_{av}=0.3, P_{IN}=25 MW) but different levels of gas dosing during the main heating phase. A second 'no-gas' BSE discharge is included (#94442), with slightly lower power (P_{IN}=20MW), that reaches lower edge density after the gas puff is switched off, resulting in very small ELMs sustained during the whole no-gas phase. Time traces are: (a) total input power (P_{IN}) and bulk radiated power, (b) edge line averaged electron density, measured by the interferometer representing $n_{e,ped}$, (c) H_{98} confinement factor, (d-f) D_α emission measured horizontally along the midplane and D_2 gas injection rate, (g) normalized beta, (h) DD neutron rate, (i) central ion and electron temperatures, (j) central toroidal rotation velocity and (k) line integrated Z_{eff}. Data in panels (i-j) are measured at $\rho_{pol} = 0.2$

density ($\langle n_e \rangle$) from far-infrared interferometry, along a vertical line of sight tangential at ρ_{pol} ~0.92 for this plasma shape, which is representative of the pedestal density, in panel (b). Here, ρ_{pol} is a label representing the square root of the poloidal flux enclosed within a given flux surface, normalized to the flux at the separatrix. The confinement enhancement factor H_{98} is plotted in panel (c). Panels (d-f) display the D_α emission signal measured horizontally along the midplane, illustrating the change in ELM dynamics, and the variation in deuterium (D) gas injection. β_N, defined as $\beta_N \equiv \beta/(I_p/aB_T)$ (% mT/MA), is plotted in panel (g). Here, $\beta = \langle P \rangle/(B^2/2\mu_0)$ is the volume-average ratio of the plasma pressure to the magnetic pressure. Panel (h) displays the neutron rate measured by the fission chambers. The central electron (T_e) and ion (T_i) temperatures are plotted in panel (i), and the plasma toroidal velocity (v_{tor}) in panel (j). The electron temperature is provided by the electron cyclotron emission (ECE) radiometer[19], while T_i and v_{tor} are measured by the active charge-exchange recombination spectroscopy (CXRS) diagnostic[20]. Data in panels (i-j) are measured at $\rho_{pol} = 0.2$. This radial location is chosen because this is the innermost point available from CXRS measurements. The last signal shown in panel (k) is the line integrated effective charge (Z_{eff}) deduced from bremsstrahlung emission.

The H-mode startup is similar in the three discharges. The application of high NBI power, at 7.5 s in this case, is soon followed by a transition to an H-mode. Access to H-mode in this scenario was controlled by using a moderate D gas injection rate ($\Gamma_D \sim 3 \times 10^{22}$ s^{-1}) during this initial phase. By starting the H-mode with high gas, long ELM-free phases were avoided, and access to a moderate edge temperature plasma with frequent ELMs is possible, avoiding an excessive increase in radiation. With the onset of the type I ELMs, the initial density rise after the L-H transition was arrested, and the edge line averaged electron density settled to a level of $\sim 5.5 \times 10^{19}$ m^{-3} (slightly lower for #94442). For discharge #94777, the initial gas level was maintained during the main heating phase, resulting in a typical ELMy H-mode, where ELMs are repetitive and density, radiation, stored energy and neutron rate become steady. For the other two discharges, soon after a stable ELMy H-mode was achieved, the D_2 gas puff was switched off for 2.5 s in the case of #94900 and 3 s for #94442. A reduction in the baseline of the D_α emission signal clearly shows the reduction in the

divertor recycling level as the gas injection is removed (see figure 1(e-f)). In the case of the discharge #94900, ELMs disappear within 0.5 s of the removal of the external gas injection, and this is correlated with a quick decrease in the edge density that drops by ∼50% of its initial value. Similar behaviour is observed for #94442, although in this case, with slightly lower NBI power, the beam fuelling is less during the no-gas phase, and the drop in the edge density is even larger (up to a ∼60% reduction). After the initial fast decrease, the pedestal and central (not shown) density reach a nearly constant level for the duration of the no-gas phase. Core line averaged electron densities are in the range of (3-3.8)$\times 10^{19}$ m^{-3} while the local density at the top of the H-mode pedestal is $\sim (1.9-2.5)\times 10^{19}$ m^{-3}. For comparison, core line averaged and pedestal densities are 7×10^{19} m^{-3} and 6×10^{19} m^{-3} in the ELMy H-mode at higher gas fuelling. The decrease in pedestal density is accompanied by an increase in pedestal temperatures, with $T_{e,ped}$ reaching values of 1.7 keV, giving a pedestal electron collisionality $\nu^*_{e,ped} = 0.10$, matching the value anticipated in ITER. Here, $\nu^*_{e,ped}$ is evaluated following the formula reported in [21]:

$$\nu^*_e = 6.921 \times 10^{-18} \frac{R q_{95} n_e Z_{eff} \ln\Lambda_e}{(a/R)^{3/2} T_e^2} \qquad (1)$$

where R, a are the major and minor radius in meters, Z_{eff} is the effective ion charge, n_e and T_e and electron density in m^{-3} and temperature in eV evaluated at the top of the pedestal and $\ln\Lambda_e$ is the Coulomb logarithm defined by $\ln\Lambda_e = 31.1\text{-}\ln(\sqrt{n_e}/T_e)$.

The resulting H-modes at lower pedestal density are characterised by the appearance of small ELMs, with an amplitude significantly smaller and at a higher frequency than those observed in conventional type I ELMy H-mode plasmas at higher pedestal density (as is the case for #94777). A key feature of this small ELMs regime is the the constant density and bulk radiated power during the no-gas phase (see figure 1(a,b)), with no core impurity accumulation, thus providing experimental evidence that plasma density and impurity content can be controlled without regular type I ELMs. A detailed description of the ELM dynamics in those conditions is provided in the next subsection. In the examples shown in figure 1, the phase at low density is stopped by the control system that initiates a pre-programmed termination sequence, which involves the use of gas puffing prior to removing the auxiliary heating power. This raises the density later in the discharge, causing the return of the larger ELMs, which last until the beam power is shut off at t =14.5 s. This termination phase is initiated at t=11 s for #94900 and t=11.9 s for #94777 and #94442. Limited attempts to extend the length of the no-gas phase have been so far unsuccessful, probably due to how the machine control system manages the plasma termination sequence in the presence of localized radiation increase on the low field side of the machine (described later in section 7). Given the limited time devoted to exploring this regime so far, it is too early to make definitive conclusions on its operational limits. This will be addressed in future dedicated experiments.

As can be seen in figure 1(i), concomitant with the density reduction, both electron and ion central temperature continuously rise during the no-gas phase at constant heating power. For these NBI-heated plasmas at low density, ion heating is dominant, and both particle and power deposition profiles from the beams are peaked at the plasma axis. Due to the low densities achieved in the absence of gas fuelling, the collisional heat transfer from ions to electrons is very small, and the central ion temperature increases more than the electron temperature, resulting in plasmas with a large ion-to-electron temperature ratio, both in the core ($T_{i0}/T_{e0} \geq 1.5$) and the pedestal region. In addition, we shall see in section 8 that there is evidence of improved ion energy confinement in these plasma conditions, which contributes to explaining the increase in the temperature ratio T_i/T_e at constant density and heating power. Not surprisingly, the toroidal rotation is seen to gradually increase in response to the decrease in density at constant injected torque, reaching a maximum level (∼400 km/s for #94900 and slightly higher for #94442) 0.5 s after the gas is switched off (see figure 1(j)). We note, however, that for #94442, the toroidal rotation increases further ($\sim$ 20%) at t =10.3 s with no change in the deposition profile or the input torque. This indicates that the momentum confinement is also improved in addition to the energy confinement during this phase. As a result of the continuous increase of central electron and ion temperatures during the no-gas phase, plasma stored energy and neutron rate slowly rise throughout that phase, with a peak neutron rate reaching values as high as 3.6×10^{16} s^{-1} in #94900 and 2.5×10^{16} s^{-1} in #94442 (figure 1(h)), significantly larger than that obtained in the standard ELMy H-mode discharge ($\sim 1 \times 10^{16}$ s^{-1}). The high-performance phase is terminated by an MHD event in the case of #94900 or by the pre-programmed gas increase in the case of #94442. For #94900, the high confinement phase is interrupted by the appearance of a medium n (in this case n=4) neoclassical tearing mode (NTM) triggered by a sawtooth crash at 10.5 s. As a result, the global performance rolls over, and the central ion temperature and the neutron rate start falling, finally saturating at a level higher than that obtained in the reference discharge with higher gas. This steady-state phase

is only finished when the gas injection is switched on again. This behaviour clearly suggests that the performance is limited by MHD rather than transport. It must be noted that this MHD event did not lead to a disruptive behaviour; the discharge survived and landed safely. The central ion temperature, neutron production and rotation begin falling immediately after the increase in density provoked by the additional gas injection at constant heating power as the plasma reverts to an ELMing H-mode, which is accompanied by a degradation of core transport properties.

It is worth mentioning that the 'no-gas' BSE regime described here has similarities with other high-performance H-mode regimes with $T_i > T_e$. Examples are the 'supershot' (L-mode) in TFTR[22] and the hot-ion ELM-free H-mode in JET with the C-wall[23]. Notably, the hot ion H-mode scenario in JET achieved the highest fusion yield transiently during the first deuterium-tritium (DTE1) campaign in 1997 [24]. Similarly to the unfuelled BSE plasmas, the hot-ion regime in JET was obtained by using high NBI power (in some cases supplemented with ICRH), in a low-recycling, low-density target plasma and achieved high central ion temperatures, high T_i/T_e, and energy confinement higher than the conventional ELMy H-mode. However, there are also clear differences. The hot ion mode in JET-C was a long ELM-free H-mode, where pedestal pressure, plasma electron density and radiation increased continuously as a function of time. The high-performance phase was, therefore, a transient effect, typically lasting <1.5 s, which was terminated by either a giant ELM followed by a back transition to L-mode or a core MHD event. This behaviour differs from observations in the 'no-gas' BSE regime where electron density and radiation remain essentially constant after the gas dosing is switched off, indicating that particle transport is fast enough to provide adequate density and impurity control, and the high performance can last up to 2 s, which corresponds to a period of 6-8 energy confinement times, and it is not limited by core accumulation or edge MHD modes.

2.2. ELM behaviour

A salient feature of the 'no-gas' BSE regime recently explored in JET is the occurrence of smaller and more frequent ELMs than those observed in discharges with higher gas injection. In the case of the discharge #94900, shortly after t=8.72 s, coinciding with the quick density drop, the type I ELMs observed in the initial phase of the discharge are replaced by very small ELMs, at a higher ELM frequency (up to f_{ELM} ~350 Hz). With the increase in pedestal pressure during the no-gas phase, largely due to an increase in pedestal temperature (not shown), ELMs at a lower ELM frequency (~55 Hz) reappear, but

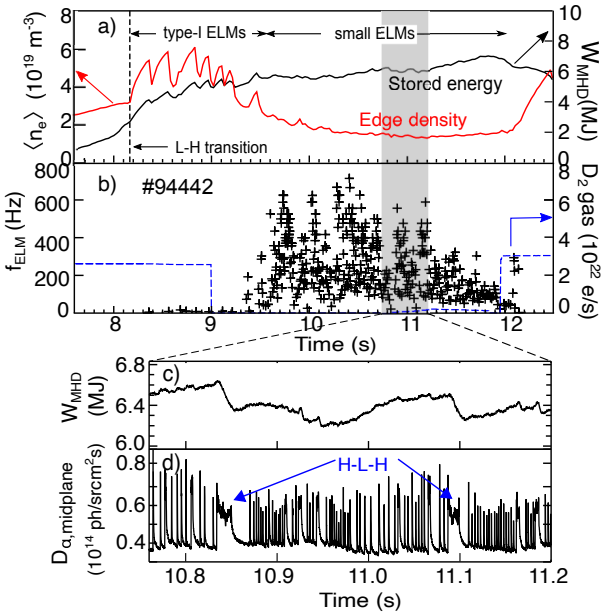

Figure 2. Time histories of (a) the edge line- averaged electron density and plasma stored energy and (b) ELM frequency for one of the H-mode discharges with no gas and small ELMs (#94442, shown in figure 1). The bottom panels show an expanded view of the shaded region in (b) to illustrate the ELM dynamics during the no-gas phase. Time traces are (c) the fast stored energy signal and (d) the D_α signal, measured horizontally along the midplane.

they remain smaller in size compared to those obtained before the gas was switched off. The energy released by the plasma during an ELM has been calculated using fast plasma stored energy data (W_{MHD}) using EFIT runs with a 0.4 ms time. The averaged ELM energy loss (ΔW_{ELM}) in #94900 decreases from 150 kJ (before the gas is switched off) to ~40 kJ (at around t=10s), while the ELM energy losses normalised to the plasma stored energy ($\Delta W_{ELM}/W_{MHD}$) decreases from ~3% to 0.48%. For comparison, the ELM frequency for the reference discharge with type I ELMs is f_{ELM}=23 Hz, with ΔW_{ELM} ~200 kJ ($\Delta W_{ELM}/W_{MHD}$ = 2.7%). When compared to the pedestal energy, the ELM energy losses decrease by almost a factor of 4 with the decrease in pedestal density, from $\Delta W_{ELM}/W_{ped}$ ~10% for #94777 to ~ 2.6% for #94900. We adopt the usual definition of the pedestal energy given by $W_{ped} = \frac{3}{2}(P_{e,ped}+P_{i,ped})\times V$, where V is the total plasma volume, and P_e and P_i are the pedestal electron and ion pressure respectively. The ion density is evaluated as $n_i = n_e(Z_{main} + 1 - Z_{eff})/Z_{main}$, assuming a spatially uniform Z_{eff} and considering beryllium as the main impurity. For this analysis, the location of the pedestal top for the electron temperature is used to evaluate both the electron and ion pedestal pressure. For the remainder of this paper, small ELMs will refer to ELMs with

$\Delta W_{ELM}/W_{ped} \leq 3\%$ and $\Delta W_{ELM}/W_{MHD} \leq 0.5\%$.

Discharge #94442 nicely illustrates how access to low edge density is a key element to open up the path for achieving small ELMs. The time history of the ELM frequency in figure 2 shows the immediate change in the ELM character (amplitude and frequency) coinciding with the decrease in the pedestal density following the gas puffing removal. In this example, the pedestal density drops to a lower value than that obtained in #94900, and the density remains fairly constant for 2 s, during which time the initial large type I ELMs disappear to be replaced by very small ELMs with an ELM frequency ranging from 600 Hz to 100 Hz, that persist for the remaining duration of the no-gas phase. The ELMs in #94442 have the smallest size obtained in the experiments reported here. The ELMs are too small to produce any measurable perturbation in the pedestal density or the temperature. At this level, ΔW_{ELM} is within the noise of the fast stored energy signal ($\sim$30 kJ), which corresponds to a maximum $\Delta W_{ELM}/W_{ped} \sim 2.5\%$. The bottom trace in figure 2 shows the recycling D_α light measured horizontally along the midplane on an expanded timescale, showing the characteristic D_α spiky behaviour introduced by the ELMs, with a sharp rise followed by an exponential decay. We can also identify short periods of H-L-H transitions, lasting less than 30 ms, triggered by a spontaneous increase in the radiated power and generally accompanied by a small decrease in stored energy ($< 5\%$) that recovered rapidly after the small ELMs reappeared.

We note that the characteristics of the small ELMs found in #94442 are reminiscent of the so-called low-density type III ELMs observed in JET-C plasmas [25], obtained at low density and with low heating power, insufficient to achieve regular type I ELMs. However, unlike the transition from the type I to type III ELMy H-mode regime in JET-C, which typically suffers from a strong degradation in energy confinement, the plasma stored energy in the discharges described here remains constant or even increases during the phase with small ELMs (see figure 2(a)). Not having information on the power dependence of the ELM frequency for the experiments described here, we will keep using the term small ELMs to refer to the ELMs found in the unfuelled BSE regime.

The presence of the short-lived H-L-H transitions shown in figure 2 indicates operation close to the H-mode power threshold (P_{LH}), despite the fact that the heating power is well above the predicted $P_{LH}^{ITPA-08}$, evaluated based on the ITPA 2008 scaling[26]. It is well-known that the $P_{LH}^{ITPA-08} \approx \overline{n}_e^{0.72} B_T^{0.80}$ does not fully capture the behaviour of the power threshold for H-mode access at lower densities. It has been observed in several devices, including JET-ILW[27, 28] that at low densities (for $n_e < n_{e,min}$), P_{LH} starts to increase as the density decreases. This is typically called the 'low-density branch' of the H-mode power threshold. If the JET-ILW plasmas in the unfuelled BSE regime operate in the 'low-density branch', the absence of large type I ELMs might be consistent with the reduction in the power margin above the P_{LH}, which is known to have a strong impact on the access to type I ELMs [25]. Unfortunately, no information on the density dependence of the P_{LH} is available for this specific combination of I_p/B_T and plasma shape, and thus we can not corroborate this hypothesis. Experiments to explore such a hypothesis were not possible in the 2019 campaigns due to time constraints and are deferred to future work.

To finish this section, it is worth noting that the radiated power and plasma density remain fairly constant after the onset of the small, high-frequency ELMs, indicating that the particle exhaust is fast enough to provide adequate density and impurity control. To identify the presence of any additional edge loss mechanism contributing to enhancing the edge particle transport, an analysis of the MHD signatures in the Mirnov coil signals during the small ELMs phase was carried out. We find low-n precursors before the large ELMs in #94442 during the initial part of the discharge before the gas is switched off, but no other MHD activity located in the edge region is observed during the no-gas phase. The ELM precursors, identified as washboard modes [29], are commonly observed in JET in discharges with low to moderate collisionality. We, therefore, conclude that the efficient W exhaust observed during the phase with no gas and small ELMs in the no-gas BSE regime is not linked to the appearance of coherent MHD activity at the edge, as is the case for the Edge Harmonic Oscillation (EHO) detected in the QH-mode[30] or the Weakly Coherence Mode (WCM) observed in the I-mode[31, 32].

2.3. Plasma performance

Operation at low density at high plasma current (3 MA) has significantly improved H-mode performance and plasma reactivity in JET-ILW. For the same heating power, the measured neutron rate in the unfuelled BSE plasmas is a factor of 2.5 or more (up to a factor of 3.5 at the peak values for #94900) higher than that in the standard ELMy H-mode, primarily due to the higher T_i attained at low density. This is confirmed by the time-dependent calculations of the neutron rate evaluated with the TRANSP code. The results of this analysis for #94900 are depicted in figure 3, where the measured total DD neutron rate is compared to the TRANSP calculations based on experimental profiles. Here, the predicted total

neutron rate is shown together with the thermal, beam-target, due to the interaction between the fast and thermal population of deuterons, and beam-beam components. Within experimental uncertainties, the calculated values agree well with the measured neutron emission and stored energy (not shown), thus providing confidence in the TRANSP results. The TRANSP predictions show that, at these high temperatures (T_{i0}=16 keV), DD neutrons production at the peak of the neutron rate is predominantly of thermonuclear origin. As shown in the figure, during this phase, ≈65% of the neutrons are produced by the thermonuclear reactions and the rest comes from beam-target reactions with a very small contribution from beam-beam reactions. We note that in the conventional baseline H-mode scenario, with higher plasma densities and $T_i \sim T_e$, the dominant mechanism of neutron production is via beam–target reactions (NBI heated dominated plasmas), but as the thermal contribution rises with increasing power the ratio between the thermal and beam induced neutron yields reaches approximate unity or slightly higher for best performing discharges at high NBI power ($>$ 28 MW) and low gas injection rate (with $T_i > T_e$) [33].

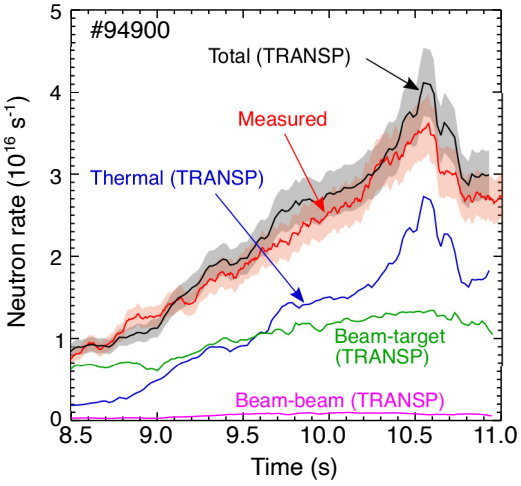

Figure 3. Comparison of the neutron rate measured (red) and predicted by TRANSP simulations (black) for discharge #94900 ('no-gas', with small ELMs). The contributions of neutrons from thermal, beam-target and beam-beam fusion reactions to the TRANSP calculated total neutron rate are indicated.

As described in the previous section, the 'no-gas' BSE discharges are characterised by low pedestal density ($n_{e,ped} < 2.5 \times 10^{19}$ m^{-3} at 3 MA) and relatively high central ion temperatures, in excess of 15 keV, with $T_{i,0}/T_{e,0} \sim 1.7$. The lowest density value obtained so far is that obtained in discharge #94442 ($n_{e,ped} = 1.9 \times 10^{19}$ m^{-3}), which reached a Greenwald fraction of $f_{GW} = \langle n_{e,0} \rangle / n_{GW}$ ~0.32, amongst the lowest ever achieved in the baseline scenario in JET-ILW. Here $\langle n_{e,0} \rangle$ is the line averaged central electron density and the Greenwald density is expressed as $n_{GW}(10^{20}\ \mathrm{m}^{-3}) = I_p/(\pi a^2)$, with I_p being the plasma current (in MA) and a the minor plasma radius. This has to be compared to f_{GW} ~0.68 for the reference gas-fuelled ELMy H-mode (#94777). Although the Z_{eff} is higher for the 'no-gas' BSE discharges, the edge electron density is lower and the pedestal electron temperatures are higher than in the type I ELMy H-mode. As a result, there is a significant reduction in the pedestal top collisionality, which decreases from $\nu^*_{e,ped}$ ~0.8 in the standard ELMy H-mode to $\nu^*_{e,ped}$ ~0.1 for the 'no-gas' BSE discharges. Another characteristic of the 'no-gas' H-mode plasmas is the low fraction of the radiated power (<30%) with no central impurity accumulation. Both radiated power and line averaged density remain constant for several energy confinement times (~ 2 s), which demonstrates that the 'no-gas' BSE regime still has adequate impurity exhaust and density control.

The 'no-gas' BSE regime exhibits remarkably good absolute and normalized performance. The global enhancement confinement factor H_{98}, excluding fast ion contribution, varies from 1.1 to 1.4 in #94900, continuously increasing throughout the no gas phase due to the increase in T_i, while an averaged H_{98} ~0.9 is found in the ELMy H-mode case (#94777). For the plasma conditions analyzed here, the fast ion contribution to the stored energy decreases from 15% to 5% as the density rises. It has to be noted that the lower density in the 'no-gas' case is contributing to the increase in the H_{98} confinement factor ($\tau_{98(y,2)} \propto \overline{n}_e^{0.41}$). However, in this particular case, there is a clear increase in the plasma stored energy for similar input heating power, driven by the increase in the ion and electron temperatures. This confinement improvement can be quantified by comparing the β_N value, which increases from 1.75 to 2.2 (peak value) with the decrease in gas fuelling, as can be seen in figure 1(g).

The origin of the improved confinement for the 'no-gas' case can be inferred from the plasma profiles shown in figure 4, where kinetic profiles for #94900 are compared with those of the reference ELMy H-mode discharge at t =10.4 s, near the peak performance for the 'no-gas' discharge. Electron density and temperature profiles are measured by the high-resolution Thomson Scattering diagnostic (HRTS)[34]. The HRTS laser repetition rate is 20 Hz. Ion temperature and toroidal rotation are obtained from CXRS data. The data points in the figure were taken within the last 20% of the ELM cycle for #94777. The fits shown combine a polynomial function to fit the data in the core region with the conventionally used modified tanh function (*mtanh*) to capture the steep pedestal in the edge region. The profiles are plotted

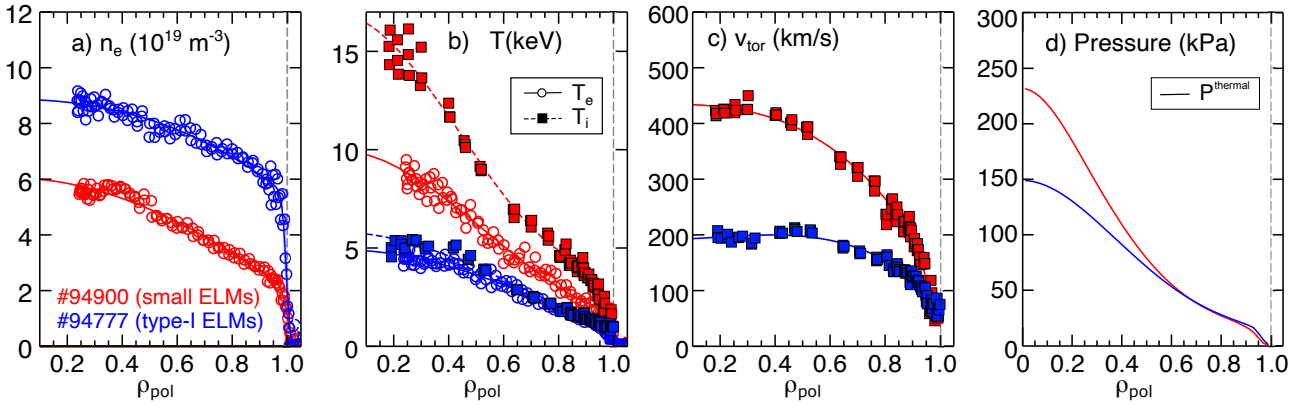

Figure 4. Radial profiles for n_e, T_e, T_i, toroidal rotation and total thermal pressure calculated by TRANSP for two of the discharges shown in figure 1 illustrating the changes in the profiles as the gas dosing is switched off, and smaller and faster ELMs replace regular type I ELMs. Profiles are compared at about t =10.4 s, near the peak performance in the 'no-gas' discharge. The data points are from Thomson Scattering (n_e,T_e), constrained by LIDAR and ECE in the plasma core, and CRXS spectroscopy (T_i, v_{tor}). Lines in (a-c) are fits to the data.

versus ρ_{pol}, where the poloidal flux is derived from a pressure constraint equilibrium using EFIT, including a correction for the fast ion pressure[35]. As shown in figure 4(a), for the 'no-gas' case, the decrease in edge density is larger than that of the core density. The net result is an increase in the density profile peaking, from ∼1.3 for #94777 to ∼1.7 for #94900, defined here as the ratio of the density at ρ_{pol}=0.3 and at ρ_{pol}=0.8. The lower density in #94900 is accompanied by an increase in pedestal temperatures ($T_{e,ped}$ ∼1.7 keV, $T_{i,ped}$ ∼ 2.4 keV, measured at the same location of $T_{e,ped}$) and improved core ion confinement, with central T_i reaching values of ∼16 keV, whereas central T_e remains below 10 keV. The total pressure (figure 4(d)) shows similar pedestal values for the type I ELMy H-mode and the 'no-gas' case, with thermal P_{ped} = 11 kPa for #94900 and 15 kPa for #94777, but noticeable higher central pressure for the discharge with small ELMs. Moreover, there is a significant increase in edge rotation that propagates all the way into the plasma centre, reaching values of ∼400 km/s in the core, whereas the rotation is significantly lower in the conventional type I ELMy H-mode. The increase in central rotation leads to a significant increase in the gradient of the rotation or shear, which is known to be beneficial for reducing turbulence transport. The impact of rotation on transport is discussed in more detail in Section 8.

3. Access to small ELMs in the unfuelled baseline scenario in JET-ILW

As described in the previous section, a characteristic feature of the 'no-gas' BSE regime is the marked reduction in ELM size compared to conventional type I ELMy H-mode plasmas. To better understand the onset conditions for the small ELMs, a dataset was compiled including discharges with similar heating power to that used by #94442 (see figure 1), but with different gas injection levels. The plasma shape, current and magnetic field were held constant in this comparison. The changes in the ELM frequency and amplitude during the gas scan are illustrated in figure 5, which shows results from three discharges, each one with a different gas injection rate. The D_α indicates the ELM frequency and the change in the fast plasma stored energy signal provides a measure of the ELM size. For this particular combination of heating power, I_p and B_T, gas dosing above 3×10^{22} D/s is typically required to obtain regular type I ELMs, as can be seen in figure 5(b). As the D_2 gas dosing is reduced to levels $< 1.5 \times 10^{22}$ D/s (see the example in figure5(b)), ELMs become too infrequent and long ELM-free H-mode phases start to develop. Impurities penetrate much more easily into the plasma during the ELM-free phases, leading to a rise in impurity concentration and radiation and eventually to core W accumulation that can be identified by the sharp rise in radiation and the drop in stored energy observed in #94446 for $t - t_0$ >9 s. Interestingly, when the gas dosing is reduced even further, plasma density decreases and the large ELMs disappear to be replaced by small ELMs at high frequencies (100-600 Hz) with a maximum estimated ELM energy loss of W_{ELM}/W_{MHD} ≤0.3%. The larger drops in plasma stored energy observed in figure 5(d) at constant heating are short H-L-H transitions indicating operation close to the H-mode power threshold, as already mentioned in section 2.2.

The impact of decreasing the gas injection rate on the pedestal parameters (pre-ELM) and ELM characteristics (ELM energy losses and frequency) is summarized in figure 6. For this analysis, we averaged

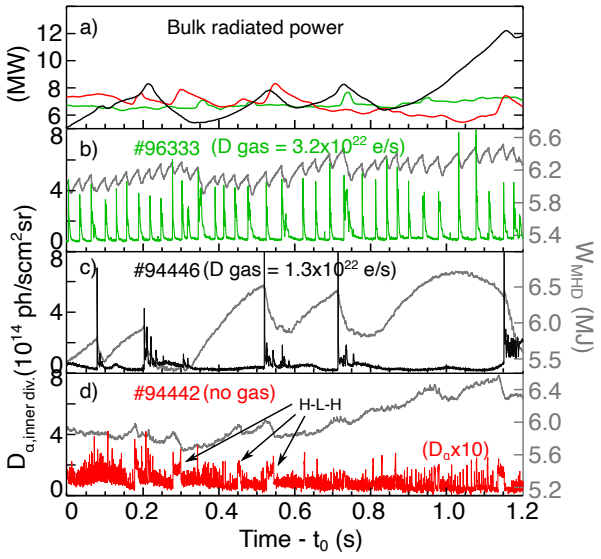

Figure 5. Comparison of 3 discharges with similar heating power and engineering parameters (as described in the text for figure 1) but different gas fuelling. We use the measured stored energy and the D_α emission from the inner divertor to illustrate the change in ELM dynamics. The bulk radiation for the three discharges is shown in the top panel. A window of 1.2 s for each of the discharges has been selected to facilitate the comparison.

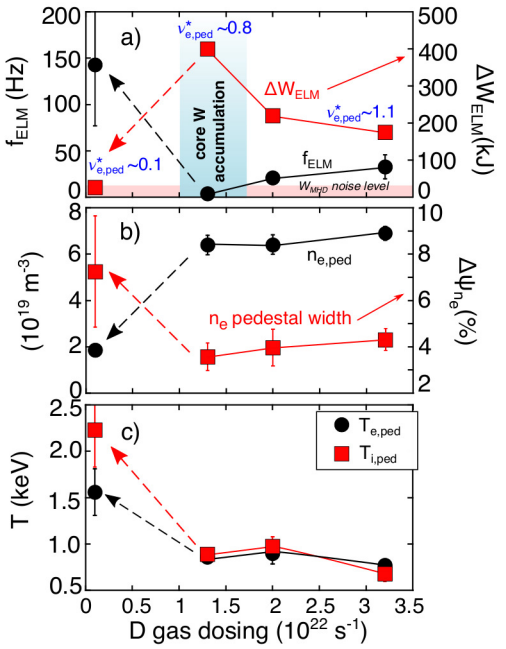

Figure 6. Changes on a) ELM frequency and ELM energy loss (ΔW_{ELM}), b) pedestal density and width and c) ion and electron pedestal temperatures during a gas scan at similar input heating power, showing the transition to the small ELMs regime at zero gas dosing. Plotted values are the result of averaging pedestal data over steady windows (1 s) of the H-mode plasmas. Engineering parameters as described in the text for figure 1.

the data over 1 s time intervals chosen such that plasma density and ELM behaviour did not vary substantially. The operational experience in JET-ILW shows that $f_{ELM} >$ 25-30 Hz is typically needed to avoid core W contamination, which is generally accomplished by operating with a certain amount of gas puffing. From figure 6(a), we can see that this minimum gas level is $\Gamma_D^{MIN} = 1.5 \times 10^{22}$ e/s for the I_P/B_T values used in these experiments. Figure 6(b) illustrates how the pedestal top density (before the ELM crash) remains largely unchanged with the increase in gas puffing, as has been seen in many tokamaks, while the pedestal cools down (see figure 6(c)), resulting in an increase in the pedestal collisionality (as noted in figure 6(a)). Above this minimum gas value, Γ_D^{MIN}, the ELM behaviour in this dataset follows the well-known trend of increasing ELM frequency and decreasing ELM size with increasing collisionality reported for type I ELMs [36]. However, this trend is reversed in the 'no-gas' BSE regime. As depicted in figure 6, when all the external gas is removed, the pedestal density height decreases and its width increases, the pedestal collisionality drops to very low levels driven by the increase in the pedestal temperature, and this is accompanied by a substantial increase in the ELM frequency and the corresponding decrease in ELM size.

From the data shown in figure 6(b), it is obvious that operation at low density and the widening of the pedestal density profile clearly correlate with the appearance of the small ELMs in the 'no-gas' BSE regime. We note a similarity with results obtained in the RMP experiments at low collisionality in AUG[37], and in the grassy ELM regime assisted by RMPs in DIII-D[38], where the suppression of type I ELMs appears to be correlated with the RMP-induced density pump-out, suggesting that the pedestal density may play an important role in the removal of the large type I ELMs. In fact, in the case of AUG, the reduction in the ELM energy losses is found to correlate with the pedestal density and not with the edge collisionality[39], with the smaller ELMs found at the lowest density. So far, no consistent explanation for reducing the ELM energy losses at low density has been found.

4. Divertor head loads and small ELMs

In this section, we report on the ELM-induced divertor heat loads measured in the JET-ILW unfuelled BSE regime, which is the key parameter to monitor in order to avoid damage to the in-vessel components in future devices, such as ITER. The impact of these transient head loads on the divertor targets plates is typically quantified by evaluating the ELM energy fluence (ϵ), defined as the peak energy density deposited on the target due to the ELMs, which is computed by time-integrating the heat flux profiles at the divertor strike

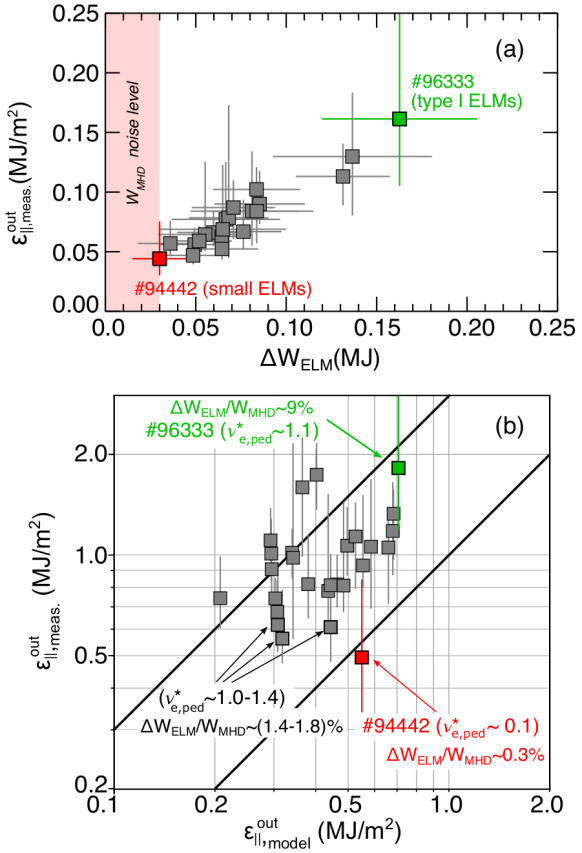

Figure 7. (a) ELM energy fluence evaluated in the outer divertor vs. ELM energy loss and (b) parallel ELM energy fluence vs. model predictions[40] for two of the discharges shown in figure 5: #94442(small ELMs, 'no-gas' BSE, red symbol) and #96333 (type I ELMs, green symbol). Those are compared with a database consisting of deuterium fuelled type I ELMy H-mode discharges (grey symbols) from a recent experiment in JET-ILW [41]. As can be seen in (b), the majority of the type I ELM data points fall within the boundaries of the lower (1:1) and upper (3:1) model boundaries.

point location for the duration of an ELM event. The divertor heat fluxes in JET are derived from infra-red (IR) thermography using a high-resolution IR camera looking vertically at the divertor target plates[42]. Details on how the ELM energy fluence is evaluated can be found in [41]. For the analysis shown here, we focus on the IR measurements on the outer strike point. Unfortunately, due to damages to the divertor tile where the outer strike point is located in these experiments, measurements for most of the small ELMs discharges are usually of insufficient quality to draw quantitative results and, so far, only one of the 'no-gas' H-mode discharges with small ELMs can be included in this study.

The results of this analysis are presented in figure 7(a), which compares the measured energy fluence ($\epsilon_{meas.}$) for two of the discharges plotted in figure 5: #94442 ('no-gas') that exhibits small ELMs and #96333 with type I ELMs. One can clearly see that the ELM energy fluence reaching the divertor surface is clearly correlated with the averaged ELM size based on the fast plasma stored energy signal. We find that, in this case, the ELM energy fluence for the discharge with small ELMs is reduced by a factor of ≈3.5 compared to the reference discharge with type I ELMs. To put those results into context, the figure also includes points of a dataset of ELMy H-mode deuterium plasmas from a recent experiment in JET-ILW[41], built using dedicated power and gas scans for a range of plasma current (I_p=1.7-2.4 MA) and toroidal magnetic field (B_T=1.7-2.8 T) values. The data shown are the result of averaging the measurements over a selected time window with constant pedestal parameters. The error bars in the energy fluence, representing the 33rd and 66th percentiles as upper and lower limits, illustrate the variability in the ELM dynamic during that period. The ELMy H-mode database spans the relative ELM energy losses from ~0.6-0.7% to 3.9%, showing the usual inverse relation of ELM losses with ELM frequency, with f_{ELM} varying between 25 Hz and 125 Hz (at high gas fuelling). We note that the ELM size determination in JET plasmas with high ELM frequencies (>70 Hz) is sometimes complicated by the appearance of a positive spike at the time of the ELM crash in the fast stored energy signal, whose origin is not yet identified, that makes it impossible to accurately extract the change in energy caused by the ELM. Those discharges are not included in figure 7(a).

To further examine the changes in the ELM behaviour observed in the 'no-gas' BSE regime, the measured ELM energy fluence is compared to that evaluated using the model developed by Eich[40] in figure 7(b). To compare with the model, the energy fluence is mapped parallel to the magnetic field ($\epsilon_{||}$), where $\epsilon_{||} \equiv \epsilon/\sin(\alpha_{\rm div})$ and $\alpha_{\rm div}$ is the angle between the divertor target and the magnetic field lines. The model, which correlates the reduction of $\epsilon_{||}$ to the reduction of the pedestal pressure height, was developed using a multi-machine data set, including measurements from MAST, AUG, and JET (both with the C-wall and the ILW) using only type I ELMy H-mode plasmas, thus a change in ELM regime to *e.g.* type III ELM or any reduction of ELM loads due to a different method is not covered by this model. As described in [41], similarly to the original dataset used to build up the model, the majority of the type I ELMy H-mode data points fall within the lower (1:1) and upper (3:1) model boundaries. We note that the model prediction was built for a dataset with $T_{i,ped} = T_{e,ped}$ and therefore it does not account for situations with $T_{i,ped} > T_{e,ped}$, as it is the case of the 'no-gas' BSE regime. Since, the temperature values

enter linearly in the model ($\epsilon_{\parallel mod.} \sim 2 \times P_{e,ped}$), the model prediction for #94442 has been evaluated by including the total pedestal pressure ($P_{i,ped} + P_{e,ped}$) taken from experimental profiles at the location of the $T_{e,ped}$ and using $n_e = n_i$ (following the same methodology used in [40]). Interestingly, the ELM energy fluence measured for the small ELMs at low collisionality in JET lies outside the confidence range of the model, overestimating the observed reduction of the ELM energy fluence for #94442 based solely on the pedestal pressure reduction. This is not surprising since the model was built up for type I ELMs, which do not match the characteristics of the small ELMs observed in the unfuelled BSE regime. In fact, one can identify clear differences between the small ELMs obtained in #94442 and those found in the gas fuelled ELMy H-mode dataset. As can be seen in the figure, the data points with the lower ELM energy fluence in the ELMy database are typically obtained in plasmas at a higher collisionality than that achieved in the 'no-gas' BSE regime and correspond to larger relative ELM energy losses.

From the trends shown in figure 7, even if based on the limited database of this first set of experiments, it is evident that the high-performance operation of the unfuelled baseline scenario in JET-ILW is compatible with the favourable property of very low divertor heat loads, much smaller than those of type I ELMs, which is essential to avoid damage to the plasma facing components in future reactors. More experiments are required to confirm our initial findings.

5. Comparison with no-gas operation in JET-C

Given that in JET with the C-wall, type I ELMs were typically observed in H-mode plasmas without external gas injection [25], the question naturally arises as to why small ELMs are now obtained in JET-ILW in the absence of external gas injection. The answer to this question resides in the very different 'natural' densities attained in JET with the different wall materials. Here we take the usual definition of the 'natural' density as the plasma density obtained in an H-mode discharge with beam fuelling but no external gas puffing. This difference is illustrated in figure 8 where one of the small ELMs discharges developed in JET-ILW is compared with a JET-C discharge at the same plasma current (3 MA) and very similar q_{95} values (q_{95}=3.1 for JET-C and 3.2 for JET-ILW) and auxiliary heating power (P_{IN} ~19-20 MW). Both discharges run with the gas valves switched off during the main heating phase. Both have a low triangularity plasma shape but the averaged triangularity is slightly lower for the JET-ILW discharge (δ_{av} ~0.20 compared to 0.25 in JET-C) owing to the different divertor

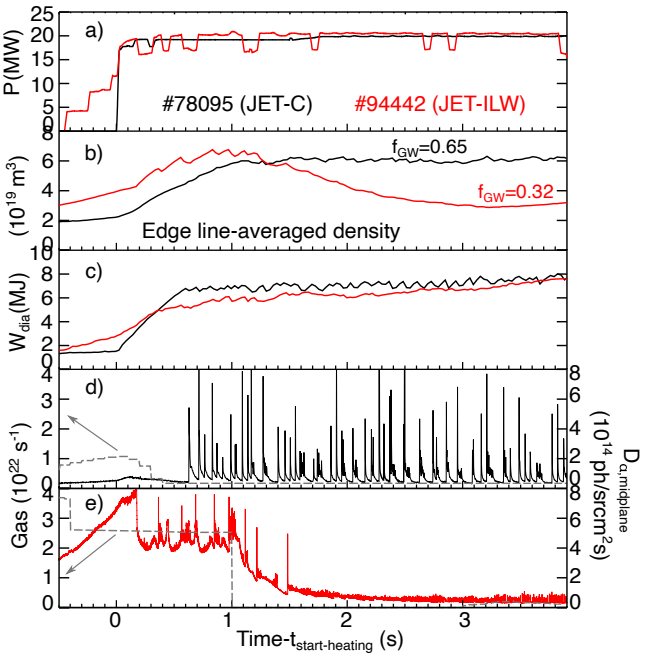

Figure 8. Comparison of JET-C and JET-ILW H-mode plasmas with similar engineering parameters (3 MA, q_{95}=3(JET-C) and 3.2(JET-ILW), slightly smaller B_T for the JET-C pulse), low triangularity, P_{IN}=19-20 MW) and no external gas fuelling during the main heating phase. Time traces are (a) total heating power, b) edge line averaged density, c) stored energy and d-e) D_α emission measured horizontally along the midplane, together with the deuterium gas injection rate (dashed lines). Note the different scales for the injected gas in (d) and (e)

geometry used in the experiments described here. The C-wall dataset at 3 MA had the outer divertor strike point in the middle of the horizontal divertor target and the inner strike point on the vertical tile, while for the ILW experiments, both the inner and outer strike points were placed in the divertor corners, close to the pumping duct (so-called divertor 'corner' configuration). The divertor geometry in the JET-C discharge allowed positioning the last close surface at a larger plasma radius; this, together with the use of smaller B_T (2.7 T instead of 2.8 T), led to a slightly smaller q_{95}=3.1. Dedicated experiments in JET-C [43] demonstrated that the impact of divertor geometry on confinement comes primarily through the different gas rates needed to match the line averaged density, which had to be increased for the discharges with stronger pumping, as it is the case of the divertor 'corner' configuration. However, these differences had almost no impact on the density behaviour in plasmas with no external gas dosing during the main heating phase. From that point of view, we are confident that the comparison shown here is relevant to address the differences in the density build-up observed in JET-C and JET-ILW plasmas with no gas injection.

As shown in figure 8, unfuelled plasmas in JET-

C naturally reach higher densities than in JET-ILW. Gas puffing beyond the L-H transition was unnecessary to maintain the H-mode plasma in stationary conditions in JET-C. With no external gas injection and with heating power well above the predicted power threshold for H-mode access, as is the case for the discharge shown here with $P_{IN}/P_{LH}^{ITPA-08}$ >1.5, the H-mode plasmas at low triangularity in JET-C were characterized by low-frequency (f_{ELM} ∼10-15 Hz), large size ELMs, with $\Delta W_{ELM}/W_{ped} \sim 16\%$. This is in contrast to the faster and smaller ELMs (with $\Delta W_{ELM}/W_{ped} \sim 2.5\%$) found in the unfuelled ILW discharge at similar heating power. It is remarkable to see the different ELM behaviour observed in the two discharges at similar pedestal collisionality, highlighting the key role played by low-density operation in accessing the small ELMs regime in JET-ILW. It is also interesting to note that the discharge with small ELMs in JET-ILW, as it evolves in time and despite achieving lower density (both core and edge), reaches stored energy values quantitatively comparable to those featured by the C-wall discharge. This is primarily due to the improved core confinement due to the reduction in turbulent transport driven by the higher T_i/T_e found in JET-ILW ($T_i = T_e$ in the case of the JET-C discharge). A discussion on the transport properties of the 'no-gas' BSE regime in JET-ILW can be found in section 8.

From the analysis of the existing dataset of unfuelled, low triangularity JET-C discharges at 3 MA, we found that the 'natural' density was in the range of 0.65-0.7 of the Greenwald density, significantly higher than that obtained in JET-ILW, with f_{GW}=0.32-0.45 for plasmas obtained with similar engineering parameters (core plasma shape, q_{95} and heating power). In the absence of gas fuelling, the build-up of the plasma density is determined by the only two remaining particle sources, namely the beam fuelling and the main chamber recycling. The lower 'natural' density in unfuelled H-mode plasmas with similar NBI power in JET-ILW compared to JET-C provides clear evidence that the wall-induced fuelling is indeed reduced in JET with the Be wall. This comparison is, therefore, consistent with the reduction in wall retention (by a factor of 10-20) achieved with the installation of the Be wall [44], typically dominated by the co-deposition of fuel in the graphite in the C-wall and in the Be in the ITER-like wall. At higher gas dosing rates, external fuelling becomes more dominant and the differences in density achieved in JET with the different wall materials become negligible[44].

6. Pedestal structure and edge stability

The differences in the pedestal structure between the small ELMs (#94442) and the reference type I ELMy H-mode (#94777) discharges are illustrated in figure 9. The figure includes the measured pedestal profiles of n_e, T_e and T_i and the total pedestal pressure ($P_{tot} = P_e + P_i$), with the ion density calculated from n_e, assuming Be as the dominant impurity. The solid lines are fits to the experimental data, using the *mtanh* function. The profile data were taken within a 1 s time window during the stationary phase of the discharges, between t=10-11 s for #94777 and close to the maximum performance for #94442 (t=11-12 s). In the case of #94777, only profiles within the last 25% of the ELM cycle were selected.

As shown in figure 9(a), operation with no gas leads to a dramatic reduction in the pedestal top density (∼ 70%). The separatrix density also decreases, with the ratio of the separatrix density to pedestal density $n_{e,sep}/n_{e,ped} \sim 20\%$ slightly lower than that found (∼30%) in the reference H-mode discharge with type I ELMs. This is accompanied by an increase in the T_e pedestal top value, with a corresponding increase in $\nabla T_{e,ped}$ in the region $0.9 \leq \psi_{pol,N} \leq 1.0$, where $\psi_{pol,N}$ is the normalized poloidal flux. Additionally, T_i significantly increase across the entire pedestal region, with T_i/T_e ∼1.5 at the location of $T_{e,ped}$, in contrast with the usual $T_{i,ped} = T_{e,ped}$ found in the conventional ELMy H-mode plasma. The large increase in pedestal temperature, in particular the ion temperature, partially compensates for the density reduction, resulting in a reduction of the pressure at the pedestal top of ∼ 40%(see figure 9(c)). The changes in the density and temperature pedestal structure result in a pressure profile which is notably wider in the discharge with small ELMs, as can be seen in figure 9(f). Both the electron density and temperature pedestals become wider as the edge density decreases, but the largest difference is observed in the density profile. The n_e pedestal top is located further inwards for the small ELMs discharge, by approximately $\Delta\psi_{pol} = 0.02$, which together with the reduction in the pedestal height leads to a substantial reduction (∼ 75%) in the maximum density gradient (see figure 9(d)). This is reflected in the pedestal pressure profile shape with a reduction of ∼50% in the peak pedestal pressure gradient.

Linear edge stability calculations have been carried out for these two cases in the framework of the peeling-ballooning (P-B) model[45, 46]. In this model, the P-B modes, which are driven unstable by the edge current density (dominated by the bootstrap current) and the pressure gradient present in the H-mode edge, are thought to be the relevant MHD instabilities in the triggering of the type I ELMs. For the analysis

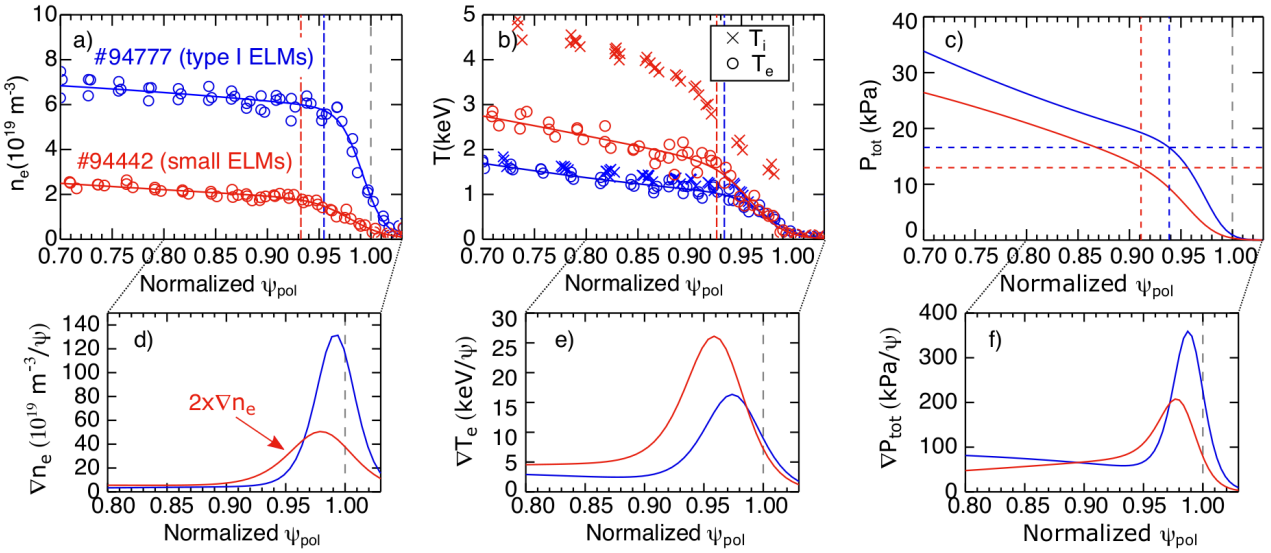

Figure 9. Pedestal profiles of #94442 (no gas, small ELMs, in red) and #94777 (type I ELMs, gas fuelled, in blue) as a function of the normalized poloidal flux: (a) electron density, (b) ion and electron temperature and (c) total pedestal pressure (thermal). Also shown are the pedestal gradients for the (d) electron density, (e) electron temperature and (f) total pressure. The density gradient for #94442 is multiplied by a factor of 2 to better visualize the differences in the pedestal profile width. The location of the pedestal, evaluated by the *mtanh* fit, is marked by vertical lines in (a-c), only for the electron temperature profile in (b). The pedestal top pressures from the *mtanh* fit are shown by the horizontal dashed lines in (c).

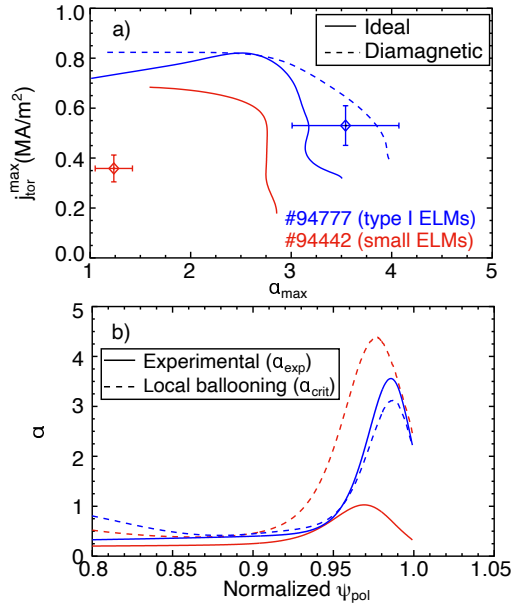

Figure 10. (a) Edge stability diagram for #94442 (small ELMs) and #94777 (type I ELMs), based on the profiles shown in figure 9. The operating experimental point is marked by the symbol with error bars. In the case of #94777, the stability boundary is evaluated with and without the ion diamagnetic drift effect. (b) Radial profiles of the ballooning stability predictions of the normalized pressure gradient, α_{crit}, (dashed line) and the experimental value α_{exp} (full line) for the same discharges.

presented here, the measured pressure profiles shown in figure 9 along with the plasma boundary from EFIT (with pressure constraints) were used as input to the HELENA equilibrium code and the stability for the P-B modes was evaluated using the ideal MHD stability code MISHKA[47]. We note that while the pedestal top and edge gradient regions are well-resolved for the n_e and T_e profiles, there are larger uncertainties in the T_i measurements in the steep gradient region close to the separatrix and the T_i profiles were fitted assuming $T_{i,sep} = T_{e,sep}$. This uncertainty has some influence in the determination of the stability limits and its proximity to the operational point of the discharge, but it does not change the main findings of the stability analysis presented here.

Figure 10(a) compares the stability analysis of the two discharges under discussion. The stability boundaries and the operational points are plotted in the usual $j - \alpha$ diagram, where j_{tor} is the flux-surface averaged edge current density and α_{max} is the peak normalized pressure gradient ($\alpha \propto R(q/B)^2 \nabla P$). The operational point is determined by the experimental profiles and marked by a symbol in the figure. The error bars indicate an uncertainty of 20% in the current density and pressure gradient. In the case of the discharge with type I ELMs (#94777), the stability boundary, including the ion diamagnetic drift, is also shown. In this case, the boundary separating stable and unstable regions is defined as $\gamma = \omega_{*i}/2$, where γ is the growth rate of the most unstable modes and ω_{*i} is the ion diamagnetic frequency. Comparison

with the ideal MHD stability limit clearly shows the stabilizing effect of the ion diamagnetic drift on the stability limits of the P-B modes in the H-mode pedestal region, which has long been found in several studies[48, 49]. By including the ion diamagnetic drift effect in the stability calculations, the stable region for #94777 is extended towards higher pressure gradients, moving the pedestal out of the unstable region and bringing the stability boundary closer to the operational point, which is consistent with the pedestal becoming unstable to P-B modes just before ELMs are triggered. Figure 10(a) shows that while the operating point of the ELMy discharge is, within the experimental errors, on the ballooning stability boundary, the pedestal of #94442 resides in the stable region, far from any stability boundary, which might explain the absence of large type I ELMs. In the case of #94442, including the diamagnetic effect (not shown) does not significantly alter the results since the operational point remains far from the stability boundary in all cases. As can be seen in figure 10(a), not only the pressure gradient but also the edge current density is smaller for the small ELMs discharge. The lower density gradient in #94222 (*i.e.,* wide pedestal) reduces the edge current, as the bootstrap drive by the density gradient is stronger compared to the temperature gradient [21], which compensates for the lower efficiency of the bootstrap drive as the collisionality increases in the case of #94777. It is interesting to note that a correlation between a wide-pedestal density and the lack of large ELMs has also been observed in some of the no-ELMs regimes that operate below the P-B stability limit, such as the QH-mode operation at low torque in double-null shaped plasmas developed in DIII-D[50] or the I-mode[51].

While the stability analysis shown here might explain why type I ELMs are not destabilised in the 'no-gas' BSE regime, the physics mechanism responsible for the appearance of the small ELMs is unknown. Recent studies in AUG indicate the key role played by the separatrix parameters in the appearance of small ELMs in the QCE regime[52]. The small ELMs in those conditions are identified as ballooning modes, which are localized close to the separatrix, driven by the local pressure gradient and stabilized by magnetic shear. To ascertain whether the same argument could be used in the 'no-gas' BSE regime, we have compared the local ballooning stability predictions of the normalized pressure gradient (α_{crit}) with the experimental value α_{exp} for the two discharges under consideration. The results of such analysis are shown in figure 10(b). In contrast to the results obtained for #94777, the experimental α_{exp} is far from the local ballooning predictions across the entire pedestal profile in the case of the small ELMs in the 'no-gas' H-mode discharge. We thus conclude that an explanation invoking unstable ballooning modes localized in the separatrix region can not be used to explain the onset of small ELMs in the no-gas BSE regime in JET. It is worth noting that the QCE regime in AUG is typically obtained in strongly fuelled plasmas and, therefore, in conditions with high separatrix density, which are very different from those found in the 'no-gas' BSE regime.

7. Impurity behaviour

Despite operation with no gas, and consequently hotter divertor target plates, and the higher electron density peaking of the 'no-gas' BSE regime, which typically leads respectively to an increase in the W source and the inward impurity convection in the core region; no evidence of central accumulation of high-Z impurities is observed throughout the high-performance phase of the small ELMs discharges, and the total radiated power is comparable to that of the reference discharge with higher gas fuelling (see figure 1(a)). Figure 11(a-b) compares the tomographic reconstruction of bolometry measurements for two of the discharges shown in figure1, one with type I ELMs and the other one with small ELMs. The figure shows very similar 2D radiation distribution, with radiation localized on the low-field-side (LFS) midplane at ρ_{pol} >0.8 and very low central values. The LFS localization of the impurities arises from neoclassical centrifugal effects that push heavy impurities towards the outside of the torus, and it is a typical feature of high NBI power, highly rotating JET discharges [53]. In the case of #94900, the density is lower, and the impurities penetrate slightly deeper into the core region (ρ_{pol} >0.65), but no signs of core accumulation are observed. The analysis of the plasma composition confirms the absence of high-Z impurities in the core region. Impurity density profiles have been determined following the methodology described in [54] that relies on the combined use of the soft X-ray, vacuum ultraviolet spectroscopy and bolometry measurements. An example of such analysis is shown in figure 11(d), where a comparison of the flux-surface averaged impurity density profiles (Be, Ni, W) for #94900 and #94777 is shown. As can be seen in the figure, Be is the dominant impurity in the core and has a density profile very similar to that of the electron density, while the mid-Z (Ni) and high-Z (W) profiles are flatter, with a tendency to become hollow as the density decreases. The W concentration in the core region remains low ($< 3 \times 10^{-5}$) for both discharges. Due to the much lower electron density at the pedestal top, the 'no-gas' discharge reaches similar radiated power to the reference with a factor of 4 increase in mid-Z (Ni/Fe/Cr/Cu) and high-Z (W) impurity concentrations, which in turn are the

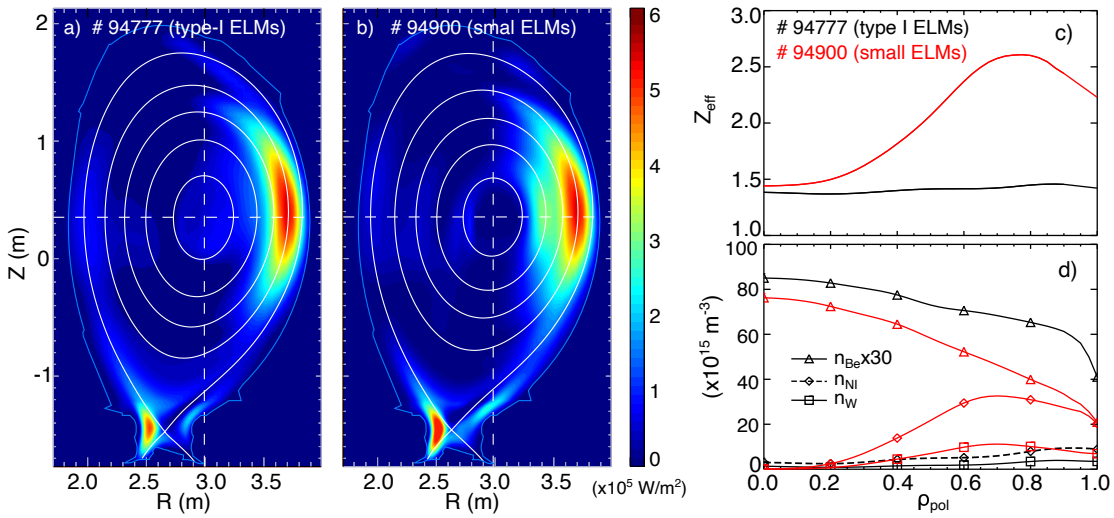

Figure 11. (a,b) 2D radiation profiles from the tomographic reconstruction of bolometric measurement showing the localization of the radiation on the plasma low field side, c) impurity profiles (W, Ni, Be) and d) Z_{eff} profiles for two of the discharges plotted in figure 1 (at t=10 s): #94777 (type I ELMs) and #94900 (small ELMs)

cause for the increased line-of-sight integrated Z_{eff} measurement (see figure 11(c)). Since the mid- and high-Z impurities are strongly localised on the LFS midplane, their increased concentration does not affect the plasma centre and the Z_{eff} profile is found to be hollow (figure 11(c)) with the central values remaining <1.5 as in the type I ELMy H-mode reference, so core dilution is also kept under control.

The lack of core impurity accumulation observed in the 'no-gas' BSE regime is consistent with recent impurity transport modelling performed using the neoclassical code NEO[55], which has identified that, under certain experimental conditions, strong plasma rotation can have a beneficial impact on the radial transport of impurities[17]. Those studies, which include the analysis of one of the 'no-gas' discharges discussed in this paper (#94442), show a reversal of the neoclassical impurity convection from inwards to outwards when plasma rotation is included in the NEO calculations, thus preventing the accumulation of impurities in the plasma core, which is in agreement with the experimental observations. It is interesting to note that previous modelling studies of the JET-ILW baseline scenario predicted a detrimental effect of plasma rotation on impurity transport. In the presence of strong plasma rotation, poloidal asymmetries appear in the W density created by centrifugal effects, which would tend to reduce the effect of the temperature screening[56]. However, the modelling and experimental results described here demonstrate that there exists an operational window where strong rotation can lead to an outward convection of impurities. The beneficial effect of the plasma rotation on the core impurity transport was first reported by Garcia and co-workers [17] and has now been further confirmed by a recent modelling work[57], which shows that the magnitude of the temperature screening can be enhanced by strong rotation in plasmas at low collisionality. In addition, the neoclassical W convection computed by NEO for the #94442 discharge also indicates the presence of a strong outward convection just above the pedestal region[17], driven by the strong ion temperature gradients developed in the pedestal region. Similar effect has also been documented in the hybrid scenario in JET-ILW[58]. In the case of the 'no-gas' BSE discharges, the substantial increase in the pedestal density width may also be a contributing factor to increasing the effective temperature screening across the pedestal region by reducing the inward-directed neoclassical convection driven by the main ion density gradient ($v_{neo} \propto \nabla n_i/n_i - 0.5 \times \nabla T_i/T_i$, where positive values correspond to a net inward transport of impurities).

8. Turbulent transport analysis

To gain insight into the physics mechanisms responsible for the good energy confinement obtained in the 'no-gas' BSE regime, a series of local gyrokinetic simulations were carried out for the three discharges shown in figure 1. The simulations were performed with the gyrokinetic code GENE [59] using experimental profiles measured during the peak performance phase of the discharges. In all cases, the calculations were performed at ρ_{tor}=0.8, where clear differences between the standard type I ELMy and the small ELMs H-mode regimes start to be noticeable. ρ_{tor} is the square root

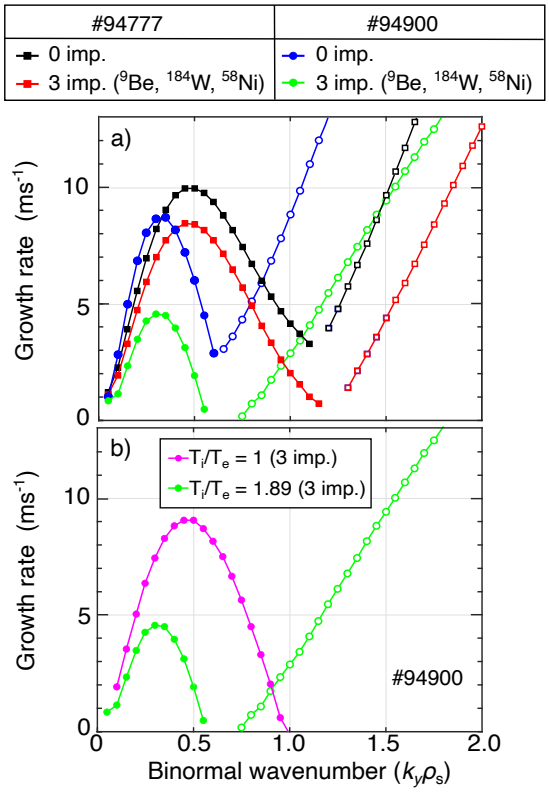

Figure 12. (a) Linear growth rate (γ) spectra obtained with the GENE code for #94777 (type I ELMs) and #94900 (small ELMs), computed at ρ_{tor}=0.8. Calculations performed with and without impurities (Be, Ni and W). Solid/open symbols denote ITG/ETG modes. (b) Comparison of the linear growth rate for #94900 with the experimental T_i/T_e value (∼1.89 at ρ_{tor}=0.8) and artificially reduced to T_i/T_e=1

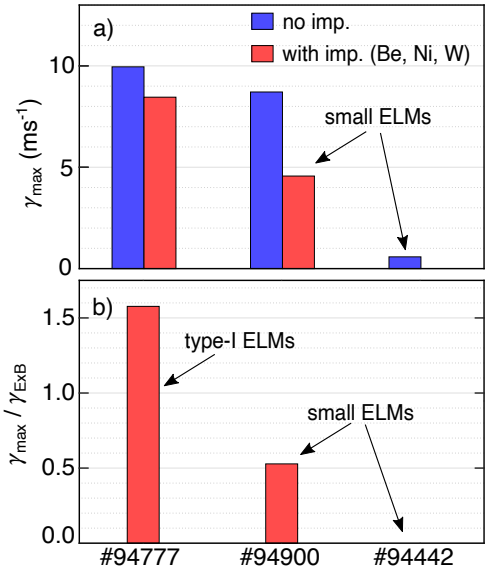

Figure 13. (a) Maximum of the turbulence growth rates and (b) $E \times B$ shear rates compared to the turbulence growth rates obtained with the GENE code computed at ρ_{tor}=0.8 for a gas fuelled, conventional ELMy H-mode plasma (#94777) and two unfuelled discharges with small ELMs, #94900 and #94442 (at lower density than #94900).

of the normalized toroidal flux. The physical parameters used as input for the gyrokinetic simulations for each of the three discharges are given in Table 1.

We will start by showing the results of the linear/local simulations, which are helpful for identifying the sensitivity of the linear growth rates to changes in parameters known to affect the underlying turbulence. The discharges investigated here, obtained with strong ion heating at low target densities, are characterized by high ion temperatures, which significantly exceed the electron temperatures. In those conditions, it is expected that the dominant instabilities are the ion temperature gradient driven instabilities (ITG). This is confirmed in figure 12, where the spectra of the growth rates (γ) of the most unstable eigenmodes for the ELMy H-mode (#94777) and one of the 'no-gas' discharges with small ELMs (#94900) are plotted as a function of the binormal wavenumber $k_y\rho_s$. Here, k_y is the perpendicular (to the magnetic field) wavenumber and $\rho_s = c_s/\Omega_{c,i}$ is the ion gyroradius evaluated as the ratio of the ion sound speed, $c_s = \sqrt{T_e/m_i}$ and the ion gyro-frequency, $\Omega_{c,i} = eB/m_i$, where m_i the ion mass. The figure shows that the dominant turbulent modes at long wavelengths are ITG modes that typically span till $k_y\rho_s < 1$. Electron temperature gradient (ETG) modes are also identified at smaller spatial scales.

Numerous studies have shown that several mechanisms can contribute to stabilising ITG driven modes. The increase in the T_i/T_e ratio is known to increase the stability of the ITG modes[60]. Another possibility is the turbulent transport being reduced by the dilution of the main ions [61]. Both effects have been explored using the GENE code, and the results of those simulations are presented in figure 12. Starting from the simplest case, where no impurities are included in the simulation, we find that the maximum growth rate of the modes at the ion scale (for $k_y\rho_s$ <1) for the 'no-gas' BSE discharge #94900 is 10% lower than the one for #94777. The T_i/T_e ratio (measured at ρ_{tor}=0.8) is∼1.89 for #94900 and is reduced to 1 for #94777 (see Table 1), a typical value for type I ELMy H-modes in JET. This is consistent with ITG theory predictions, which show that an increase of T_i/T_e would increase the critical gradients for the onset of the ITG modes [60]. We repeated the analysis taking into account the impurities located at the plasma edge (Be, Ni and W), blocked by the positive pinch from the neoclassical transport. The results of those simulations, also plotted in figure 12(a), show a significant decrease in the maximum growth rate of the modes compared to the case without impurities. We found that while including impurities reduced the maximum growth rate for both discharges, the impact is higher with increasing T_i/T_e ratio and, therefore, is stronger for #94900, with the peak of the growth rate reduced by 50%. This

Table 1. Physical parameters used in the GENE simulations discussed in section 8, evaluated at ρ_{tor}=0.8. Here ρ_{tor} is the square root of the normalized toroidal flux, q the safety factor, $\hat{s}$ the magnetic shear, the logarithmic gradients are defined as $L_X = X/\nabla X$, where $X = (n_{e,i}, T_e, T_i)$, $n_{e,i}$ is the electron and ion density and $T_{e,i}$ the electron and ion temperature, R is the plasma major radius, n_D is the deuterium density, n_{Be} is the beryllium density, n_{Ni} is the nickel density and n_W is the tungsten density

shot no.	q	$\hat{s}$	T_i/T_e	$R/L_{n_{e,i}}$	R/L_{T_e}	R/L_{T_i}	n_D/n_e	n_D/n_{Be}	n_D/n_{Ni}	n_D/n_W
#94442	2.12	1.77	2.37	1.74	3.66	2.71	0.82	0.020	0.0020	0.00050
#94900	2.09	1.82	1.89	2.46	5.13	4.67	0.87	0.016	0.0015	0.00033
#94777	2.07	1.72	1.00	1.07	6.28	6.28	0.90	0.022	0.0002	0.00007

points to the important role of the pedestal as a source of improved core confinement. These findings are consistent with earlier studies performed in highly radiating scenarios in JET, where the injection of neon was found to contribute to the ITG mode stabilization via ion dilution[62]. To further examine the influence of the T_i/T_e ratio on the turbulent transport, tests were made by artificially decreasing T_i in the simulations. The result of this analysis for the discharge #94900 is shown in figure 12(b), where T_i/T_e was varied from 1.89 (from experimental data) to 1.0. One can see that the reduction of T_i leads to a massive increase in the mode growth rate.

The next step in this analysis was to determine the impact of the higher rotation found in the 'no-gas' BSE case on the ITG turbulence. The increase in the core toroidal velocity and its gradient (see figure 4) leads to an increase in the $E \times B$ shear, which is believed to play an important role in reducing or even suppressing the turbulence-driven transport in the ITG regime[63]. To quantify the efficacy of this suppression mechanism, the $E \times B$ shearing rate is typically compared to the maximum linear growth rates of the unstable modes. The normalized perpendicular shearing rate ($\gamma_{E\times B}$) is defined in GENE as $\gamma_{E\times B} = (r/q)(\mathrm{d}\Omega/\mathrm{d}r)/(c_s/a)$, where q is the local value of the safety factor, r the radial coordinate, Ω the toroidal angular velocity, c_s is the ion sound speed defined above and a the minor radius. The results of this analysis are plotted in figure 13, this time including the discharge #94442, at lower density and with the smallest ELM size. As seen in figure 13(a), the linear growth rate for #94442 is quite low compared to the other two discharges. In this case, the turbulent transport is nearly suppressed due to the high T_i/T_e in the pedestal, which has an important stabilizing effect for the ITG modes and is consistent with the linear gyrokinetic results shown in figure 12(b). The turbulence response to the $E \times B$ shear is plotted in figure13(b). The $E\times B$ shearing rate for #94900 significantly exceeds the linear growth rate of the most unstable modes, with $\gamma_{max}^{94900}/\gamma_{E\times B}$ ~0.5, thus achieving the conditions required for turbulence stabilisation, even reaching full turbulence suppression for #94442.

In summary, our linear study has identified three main mechanisms contributing to the reduced ITG turbulence and hence the improved confinement observed in the 'no-gas' BSE regime, namely the high T_i/T_e ratio in the core and pedestal regions, the increased $E \times B$ shear driven by the strong core rotation and the ion dilution due to localized presence of impurities at the plasma edge. Our findings support those reported in [17], where similar trends were found in non-linear gyrokinetic simulations of the fuelled (low gas with pellets) BSE regime. In those simulations, the mechanisms at play leading to a reduction in the turbulent transport in the non-linear analysis were essentially the same as those identified in the linear simulations. This clearly indicates that in the plasma conditions relevant to the BSE regime, for both fuelled and unfuelled cases, the underlying linear physics carries over into the fully developed nonlinear turbulent state. The importance of the aforementioned mechanisms in the resulting transport has also been confirmed by integrated modelling of Neon seeded baseline discharges in JET, including both low [64] and high[65] neon injection levels.

The results of the simulations shown here illustrate the complex interplay between core and edge plasma regions leading to the improved confinement found in the 'no-gas' BSE discharges. Operation at low edge density allows access to a pedestal with a high T_i/T_e ratio. This results in a decrease in the turbulent transport in the ITG regime, amplified by the impurity-induced turbulence reduction due to the enhanced radiation localized at ρ_{pol} >0.8. This reduction of turbulent transport, which starts at the pedestal top, increases T_i that propagates to the core region, facilitating the achievement of high core performance. At the same time, the increased core rotation allows the $E \times B$ shear to stabilise the ITG modes, allowing the ion temperature gradients to increase further, which in turn increases the T_i/T_e ratio in the core, building up a self-amplifying feedback transport loop. We note that, as described in section 6, the reduced pedestal density gradient allows for achieving high pedestal temperatures while still operating below the ELM stability limit. In the context of the P-B model, we speculate that there is still a margin for further increasing the

pedestal temperatures with additional heating power while maintaining the pressure gradient stable to P-B instabilities. This could be utilised as an additional knob to boost the core confinement while still avoiding triggering large type I ELMs and will be explored in future dedicated experiments.

9. Discussion and future work

A new H-mode regime at low density and low q_{95} (=3.2, with I_p=3 MA) that simultaneously achieves the desired properties of good energy confinement (H_{98}=1-1.4 and β_N=1.8-2) with small ELMs at low pedestal collisionality (ν^*_{ped} ~0.1, similar to that expected in ITER) has been discovered in JET-ILW. ELM energy losses in those plasma conditions are less than 3% of the pedestal stored energy. Such a regime is obtained by completely removing the external gas injection, leading to a decrease in the edge density and a substantial increase in rotation and ion and electron temperatures in the pedestal and the core region. Noteworthy differences in plasma performance when compared to the conventional type I ELMy H-mode regime, which in the case of JET-ILW typically includes a minimum gas injection ($> 1.5\times10^{22}$ e/s for plasmas at I_p=3 MA) for W control, are higher pedestal and core temperatures, higher reactivity with $T_i > T_e$, lower collisionality and significant reduction in the ELMs size and the associated divertor heat loads. It is worth noting that the experiments reported here are the first in JET-ILW where unfuelled H-mode operation has led to sustained H-mode plasmas for several energy confinement times with good energy confinement and no accumulation of impurities in the core region. Comparison with unfuelled H-modes plasmas in JET-C has revealed that the Be-wall's lower wall retention allows access to a low-density regime that was not accessible with the C-wall, which explains why this regime was not discovered sooner. It is worth emphasizing that access to the low pedestal collisionality anticipated in ITER is particularly challenging in metal wall devices, and therefore this newly found regime has provided a valuable opportunity to investigate (a) the onset conditions for small ELMs with pedestal temperature and density profiles substantially different from those obtained in the conventional ELMy H-mode regimes and (b) the different mechanisms of turbulence stabilization and impurity transport control in high-temperature plasmas, at the low collisionality values expected for ITER.

The good confinement in the 'no-gas' BSE regime appears to result primarily from the ability to operate at low pedestal density ($\leq 2\times10^{19}$ m^{-3}) and high NBI power (>20 MW) at high plasma current (3 MA). In the absence of external gas fuelling, low pedestal density can be achieved in JET-ILW, resulting in higher pedestal ion and electron temperature (up to a factor of 2 larger for $T_{i,ped}$) than those typically found in ELMy H-mode plasmas. Both rotation and the elevated pedestal temperatures contribute to the high core confinement obtained in this regime. A centrally peaked low target density allows for a more central deposition of power and particles by NBI, that decouples electrons and ions, resulting in higher T_i/T_e ratios than standard baseline scenarios. But while this is an important ingredient, other physics aspects contribute to the observed good performance. Gyrokinetic analysis indicates that the confinement improvement is correlated with a reduction in the turbulent transport, which starts from the pedestal region and is due to the combined effect of the stabilization of ITG turbulence driven by the high T_i/T_e ratio, the impurity-induced reduction of turbulent at the plasma edge and the suppression of turbulence arising from the E×B shear flow. This is common to the fuelled (low gas and pellets)[17] and the unfuelled BSE regime described in this paper. Recently, the gyrokinetic analysis for the BSE regime (both fuelled and unfuelled) was extended to include the pedestal top location[66], identifying clear differences between the type I ELMy H-mode and the BSE regimes. While kinetic-ballooning modes(KBM) were destabilized at $k_y\rho_s \sim 0.1$ in the type I ELM regime, they were stable in the BSE discharges. Nonlinear simulations are ongoing and will be presented elsewhere.

Regarding the impurity behaviour in the 'no-gas' BSE discharges, the unique characteristics of this regime, with peaked density profiles, steep ion temperature gradients in the pedestal region and high NBI power, have provided an excellent platform to test key aspects of the neoclassical predictions of the impurity transport. In particular, these experiments have provided strong experimental evidence for the beneficial effect of rotation on impurity transport in plasmas at low collisionality[17, 57] and the appearance of outward convection at the edge of the plasma driven by enhanced temperature screening, similar to that expected in ITER[67]. Impurity transport modelling results[17] are consistent with the lack of W core accumulation observed in this operating regime.

Unfuelled H-mode operation in JET-ILW at low q_{95} is found to be naturally stable against large ELMs. Comparison with the P-B modes stability model indicates that the combination of a reduced pedestal pressure gradient (mainly driven by the large decrease in the density gradient) and the concomitant decrease in the edge current density makes the edge plasma stable with respect to the P-B modes. The reduced pedestal density gradient allows for achieving

high pedestal temperatures while still operating below the type I ELM stability limit. This allows access to the low pedestal collisionality values (ν^*_{ped} ~0.1) expected in ITER while at the same time keeping the ELM-driven divertor heat loads to an acceptable level ($\Delta W_{ELM}/W_{ped}$ ≤2% with $\epsilon^{out}_{\parallel} \leq 0.5$ MJ/m^2). The main interest of the 'no-gas' BSE regime developed in JET-ILW resides in the fact that the small ELMs are achieved in plasma conditions where the ITER baseline scenario targets of $\nu^*_{e,ped}$, β_N, H_{98} and q_{95} are simultaneously matched, which makes it very different from other small ELMs regimes, typically obtained at higher q_{95} and higher collisionality. Understanding the underlying physics mechanisms controlling the access to small ELMs in plasmas with high pedestal temperatures is important for developing suitable small ELMs regimes compatible with the confinement requirements of future tokamaks such as ITER. Outstanding challenges in terms of reactor relevance include low-density operation, with $f_{GW} = 0.3 - 0.4$ compared with the ITER baseline scenario ($f_{GW} \sim 0.85$) and the compatibility with divertor detachment. Despite the challenges mentioned above, one aspect of this regime that makes it particularly relevant for ITER is worth highlighting. In the absence of gas injection, the transport in the pedestal region of 'no-gas' BSE regime is basically determined by turbulent and neoclassic transport. This is an especially important topic to investigate since in future fusion devices, like ITER, fuel penetration beyond the separatrix, from gas, edge recycling or even from pellets, will be much weaker than in present devices. In this context, the unfuelled BSE regime provides a unique opportunity to study the 'natural' transport in the pedestal region in the absence of edge particle sources, including low wall recycling due to the Be-wall. These plasmas can, therefore, be used as a tool for investigating the role of source vs. transport in forming the pedestal density, which is clearly of interest for both present and future devices.

To date, what causes the onset of the small ELMs at low collisionality in JET-ILW remains an open question and is the subject of ongoing study. This is very different from the usual type I ELM phenomenology, where the ELM energy losses are found to increase with decreasing collisionality[36]. The experiments show that the lower pedestal density height and gradient play the most important role in determining access to small ELMs in JET. The lack of large ELMs and the lower pedestal pressure gradient, mostly due to the development of a wider pedestal density profile, indicate that we are exploring a different part of the edge stability operating space than the conventional ELMy H-mode. Moreover, the achievement of stationary operation for density and impurities in the absence of type I ELMs shows that particle transport is fast enough for density control and impurity exhaust. We note similarities with ELM-less plasma regimes that operate at relatively low densities, such as the I-mode[31, 32] or the QH-mode[30], which show neither large ELMs nor impurity accumulation and operate at constant density and radiated power. The working hypothesis in those cases is that MHD modes appearing at the plasma edge (*e.g.* the EHO in the QH-mode or the WCM in the I-mode) are responsible for providing additional particle transport, thus preventing the plasma edge from approaching the peeling-ballooning limit. However, such an explanation can not be invoked in the case of the 'no-gas' BSE regime in JET-ILW, where no edge MHD activity has been observed. Therefore, different physic mechanisms must be responsible for regulating the edge transport and keeping the plasma density stationary in the absence of ELMs, which have not yet been identified. The current H-mode theory posits that a transport barrier is maintained in the pedestal region through turbulence suppression via radially sheared $E \times B$ flows driven by the strong pressure gradients. In this context, one could put forward the argument that the decrease in the pressure gradient in the unfuelled BSE regime could be the consequence of a change in the edge turbulence and the $E \times B$ shear, for example, via a weakening in the transport barrier that would cause the edge turbulence to increase. But, as pointed out in [68], this mechanism will affect all transport channels and, therefore, will not be compatible with the high pedestal temperature gradients consistently observed in the 'no-gas' BSE regime. Further work is therefore needed to understand the nature and characteristics of the transport processes responsible for modifying the particle transport at the plasma edge while leaving the heat transport unaffected.

It is interesting to note that some of the features found in the 'no-gas' BSE regime in JET are similar to those of the I-mode regime. The I-mode regime is obtained at powers below the L-H power threshold, in conditions where the P_{LH} is kept high (unfavourable ion ∇B drift direction), and the particle and heat transport are found to be decoupled[31, 32]. In a similar fashion to the results obtained in the 'no-gas' BSE regime, in the I-mode a pedestal is built up in the temperature but not in the density, with its gradient reduced to levels close to those found in L-mode. The similarities and differences between these two operating regimes certainly deserve further investigation, which might help to better understand the underlying physics that independently controls the energy and particle transport channels.

It is worth mentioning that the H-mode regime with small ELMs at low collisionality is a new

finding in JET, and the database is still very limited. In these initial experiments, there was little time for exploring the operational space of this regime. Dedicated experiments are foreseen in JET, which will further investigate the performance limits and pedestal stability of 'no-gas' BSE regime and compare with other small ELMs regimes currently being investigated at JET.

Acknowledgments

This work has been carried out within the framework of the EUROfusion Consortium, funded by the European Union via the Euratom Research and Training Programme (Grant Agreement No 101052200 — EUROfusion). Views and opinions expressed are, however, those of the author(s) only and do not necessarily reflect those of the European Union or the European Commission. Neither the European Union nor the European Commission can be held responsible for them. This research was partly supported by the PID2021-127727OB-I00 grant funded by the Spanish Ministry of Science and Innovation. The gyrokinetic simulations were performed on CINECA Marconi HPC within the EUROfusion project WPJET1.

References

[1] Loarte A. *et al* 2007 Transient heat loads in current fusion experiments, extrapolation to ITER and consequences for its operation *Physica Scripta* **T128** 222

[2] Viezzer E. 2018 Access and sustainment of naturally ELM-free and small-ELM regimes *Nuclear Fusion* **58** 115002

[3] Evans T. E. *et al* 2004 Suppression of Large Edge-Localized Modes in High-Confinement DIII-D Plasmas with a Stochastic Magnetic Boundary *Phys. Rev. Lett.* **92**(23) 235003

[4] Suttrop W. *et al* 2018 Experimental conditions to suppress edge localised modes by magnetic perturbations in the ASDEX Upgrade tokamak *Nuclear Fusion* **58**(9) 096031

[5] Jeon Y. M. *et al* (KSTAR team) 2012 Suppression of Edge Localized Modes in High-Confinement KSTAR Plasmas by Nonaxisymmetric Magnetic Perturbations *Phys. Rev. Lett.* **109**(3) 035004

[6] Sun Y. *et al* 2016 Nonlinear Transition from Mitigation to Suppression of the Edge Localized Mode with Resonant Magnetic Perturbations in the EAST Tokamak *Phys. Rev. Lett.* **117**(11) 115001

[7] Kamada Y. *et al* 2000 Disappearance of giant ELMs and appearance of minute grassy ELMs in JT-60U high-triangularity discharges *Plasma Physics and Controlled Fusion* **42** A247–A253

[8] Saibene G. *et al* 2005 Characterization of small ELM experiments in highly shaped single null and quasi-double-null plasmas in JET *Nuclear Fusion* **45** 297

[9] Yang Q. *et al* 2020 Stationary high-performance grassy ELM regime in EAST *Nuclear Fusion* **60** 076012

[10] Wang Y. *et al* 2020 Grassy ELM regime at low pedestal collisionality in high-power tokamak plasma *Nuclear Fusion* **61** 016032

[11] Faitsch M. *et al* 2021 Broadening of the power fall-off length in a high density, high confinement H-mode regime in ASDEX Upgrade *Nuclear Materials and Energy* **26** 100890

[12] Oyama N. *et al* 2005 Energy loss for grassy ELMs and effects of plasma rotation on the ELM characteristics in JT-60U *Nuclear Fusion* **45** 871

[13] Neu R. *et al* 2005 Tungsten: an option for divertor and main chamber plasma facing components in future fusion devices *Nuclear Fusion* **45** 209

[14] Neu R. *et al* 2013 First operation with the JET International Thermonuclear Experimental Reactor-like wall *Physics of Plasmas* **20** 056111

[15] Garzotti L. *et al* 2019 Scenario development for D–T operation at JET *Nuclear Fusion* **59** 076037

[16] Mailloux J. *et al* 2022 Overview of JET results for optimising ITER operation *Nuclear Fusion* **62** 042026

[17] Garcia J. *et al* 2022 New H-mode regimes with small ELMs and high thermal confinement in the Joint European Torus *Physics of Plasmas* **29** 032505

[18] ITER Physics Expert Group on Confinement and Transport, ITER Physics Expert Group on Confinement, Modelling and Database and ITER Physics Basis Editors 1999 Chapter 2: Plasma confinement and transport *Nuclear Fusion* **39** 2175

[19] de la Luna E. *et al* 2004 Electron cyclotron emission radiometer upgrade on the Joint European Torus (JET) tokamak *Rev. Sci. Instrum.* **75** 3831–3834

[20] Hawkes N. C. *et al* 2018 Instrumentation for the upgrade to the JET core charge-exchange spectrometers *Review of Scientific Instruments* **89** 10D113

[21] Sauter O., Angioni C. and Lin-Liu Y. 1999 Neoclassical conductivity and bootstrap current formulas for general axisymmetric equilibria and arbitrary collisionality regime *Physics of Plasmas* **6** 2834–9

[22] Strachan J. D. *et al* 1987 High-temperature plasmas in a tokamak fusion test reactor *Phys. Rev. Lett.* **58**(10) 1004–1007

[23] The JET Team (presented by T.T.C. Jones) 1995 The route to high performance on JET *Plasma Phys. Control. Fusion* **37** A359

[24] Keilhacker M. *et al* 1999 High fusion performance from deuterium-tritium plasmas in JET *Nuclear Fusion* **39** 209–234

[25] Sartori R. *et al* 2004 Study of Type III ELMs in JET *Plasma Physics and Controlled Fusion* **46** 723

[26] Martin Y. R., Takizuka T. and the ITPA CDBM H-mode Threshold Database Working Group 2008 Power requirement for accessing the H-mode in ITER *Journal of Physics: Conference Series* **123** 012033

[27] Maggi C. *et al* 2014 L–H power threshold studies in JET with Be/W and C wall *Nuclear Fusion* **54** 023007

[28] Solano E. *et al* 2022 Recent progress in L–H transition studies at JET: tritium, helium, hydrogen and deuterium *Nuclear Fusion* **62** 076026

[29] Perez C. *et al* 2004 Type-I ELM precursor modes in JET *Nuclear Fusion* **44** 609

[30] Burrell K. H. *et al* 2002 Quiescent H-mode plasmas in the DIII-D tokamak *Plasma Physics and Controlled Fusion* **44** A253

[31] Whyte D. *et al* 2010 I-mode: an H-mode energy confinement regime with L-mode particle transport in Alcator C-Mod *Nuclear Fusion* **50** 105005

[32] Happel T. *et al* 2017 The I-mode confinement regime at ASDEX Upgrade: global properties and characterization of strongly intermittent density fluctuations *Plasma Physics and Controlled Fusion* **59** 014004

[33] Štancar Ž. *et al* 2023 Overview of interpretive modelling of fusion performance in JET DTE2 discharges with

TRANSP *Nuclear Fusion* **63** 126058
[34] Pasqualotto R. *et al* 2004 High resolution Thomson scattering for Joint European Torus (JET) *Review of Scientific Instruments* **75** 3891–3893
[35] Szepesi G. *et al* 2021 Advanced equilibrium reconstruction for JET with EFIT++ *47th EPS Conference on Plasma Physics, Stiges, Spain* vol P3.1037
[36] Loarte A. *et al* 2003 Characteristics of type I ELM energy and particle losses in existing devices and their extrapolation to ITER *Plasma Physics and Controlled Fusion* **45** 1549
[37] Suttrop W. *et al* 2017 Experimental studies of high-confinement mode plasma response to non-axisymmetric magnetic perturbations in ASDEX Upgrade *Plasma Physics and Controlled Fusion* **59** 014049
[38] Nazikian R. *et al* 2018 Grassy-ELM regime with edge resonant magnetic perturbations in fully noninductive plasmas in the DIII-D tokamak *Nuclear Fusion* **58** 106010
[39] Leuthold N. *et al* 2017 Parameter dependence of ELM loss reduction by magnetic perturbations at low pedestal density and collisionality in ASDEX upgrade *Plasma Phys. Control. Fusion* **59** 055004
[40] Eich T. *et al* 2017 ELM divertor peak energy fluence scaling to ITER with data from JET, MAST and ASDEX upgrade *Nuclear Materials and Energy* **12** 84–90
[41] Faitsch M. *et al* 2023 Divertor power load investigations with deuterium and tritium in type-I ELMy H-mode plasmas in JET with the ITER-like wall *Nuclear Fusion* **63** 112013
[42] Balboa I. *et al* 2023 Remote infrared view of JET divertor compatible with D-T operations *Plasma Physics and Controlled Fusion* **65** 094002
[43] de la Luna E. *et al* 2014 Comparative study of high triangularity H-mode plasma performance in JET with Be/W wall and CFC wall *Proc. 25*$^{\text{th}}$ *IAEA Fusion Energy Conference, Saint Petersburg, October 2014*
[44] Brezinsek S. *et al* 2013 Fuel retention studies with the ITER-Like Wall in JET *Nuclear Fusion* **53** 083023
[45] Connor J. W., Hastie R. J., Wilson H. R. and Miller R. L. 1998 Magnetohydrodynamic stability of tokamk edge plasma *Physics of Plasmas* **5**(7) 2687–2700
[46] Snyder P. B. *et al* 2002 Edge localized modes and the pedestal: A model based on coupled peeling–ballooning modes *Physics of Plasmas* **9**(5) 2037–2043
[47] Mikhailovskii A. B., Huysmans G. T., Kerner W. O. and Sharapov S. E. 1997 Optimization of computational MHD normal-mode analysis for tokamaks *Plasma Physics Reports* **23**(10) 844–857
[48] Huysmans G. T. A., Sharapov S. E., Mikhailovskii A. B., and Kerner W. 2001 Modeling of diamagnetic stabilization of ideal magnetohydrodynamic instabilities associated with the transport barrier *Physics of Plasmas* **8**(10) 4292
[49] Aiba N. 2016 Impact of ion diamagnetic drift on ideal ballooning mode stability in rotating tokamak plasmas *Plasma Phys. Control. Fusion* **58** 045020
[50] Chen X. *et al* 2016 Stationary QH-mode plasmas with high and wide pedestal at low rotation on DIII-D *Nuclear Fusion* **57** 022007
[51] Walk J. R. *et al* 2014 Edge-localized mode avoidance and pedestal structure in I-mode plasmasa *Physics of Plasmas* **21** 056103
[52] Radovanovic L. *et al* 2022 Developing a physics understanding of the quasi-continuous exhaust regime: pedestal profile and ballooning stability analysis *Nuclear Fusion* **62** 086004
[53] Angioni C. *et al* 2014 Tungsten transport in JET H-mode plasmas in hybrid scenario, experimental observations and modelling *Nuclear Fusion* **54** 083028
[54] Sertoli M., Carvalho P., Giroud C., Menmuir S. and Contributors J. 2019 Measuring the plasma composition in tokamaks with metallic plasma-facing components *Journal of Plasma Physics* **85** 905850504
[55] Belli E. A. and Candy J. 2008 Kinetic calculation of neoclassical transport including self-consistent electron and impurity dynamics *Plasma Physics and Controlled Fusion* **50** 095010
[56] Angioni C. *et al* 2015 The impact of poloidal asymmetries on tungsten transport in the core of JET H-mode plasmas *Physics of Plasmas* **22** 055902[
[57] Fajardo D. *et al* 2023 Analytical model for the combined effects of rotation and collisionality on neoclassical impurity transport *Plasma Physics and Controlled Fusion* **65** 035021
[58] Field A. *et al* 2022 Peripheral temperature gradient screening of high-Z impurities in optimised 'hybrid' scenario H-mode plasmas in JET-ILW *Nuclear Fusion* **63** 016028
[59] Jenko F., Dorland W., Kotschenreuther M. and Rogers B. N. 2000 Electron temperature gradient driven turbulence *Physics of Plasmas* **7** 1904–1910
[60] Romanelli F. 1998 Ion temperature-gradient-driven modes and anomalous ion transport in tokamaks *Physics of Fluids B: Plasma Physics* **1** 1018
[61] McKee G. *et al* 2000 Impurity-Induced Suppression of Core Turbulence and Transport in the DIII-D Tokamak *Phys. Rev. Lett.* **84**(9) 1922–1925
[62] Glöggler S. *et al* 2019 Characterisation of highly radiating neon seeded plasmas in JET-ILW *Nuclear Fusion* **59** 126031
[63] Burrell K. H. 1997 Effects of E×B velocity shear and magnetic shear on turbulence and transport in magnetic confinement devices *Physics of Plasmas* **4** 1499–1518
[64] Gabriellini S. *et al* 2023 Neon seeding effects on two high-performance baseline plasmas on the Joint European Torus *Nuclear Fusion* **63** 086025
[65] Giroud C. *et al* 2021 High performance ITER-baseline discharges in deuterium with Nitrogen and Ne seeding in JET-ILW *28th IAEA Fusion Energy Conference, Nice, France (remote meeting)*
[66] Dicorato M. *et al* 2022 Gyrokinetic Stability Analysis of JET Pedestal Top Plasmas with Small-ELMs *Journal of Physics: Conference Series* **2397** 012007
[67] Dux R., Loarte A., Fable E. and Kukushkin A. 2014 Transport of tungsten in the H-mode edge transport barrier of ITER *Plasma Physics and Controlled Fusion* **56** 124003
[68] Manz P. *et al* 2020 Physical mechanism behind and access to the I-mode confinement regime in tokamaks *Nuclear Fusion* **60** 096011